A STATISTICAL STUDY OF THE CONTAMINANT DEPOSITION FROM A JET AND BEHIND A MOVING PERSON

by

Autumn Noël Weber

Submitted in Partial Fulfillment
of the Requirements for the Degree of
Master of Science in Mechanical Engineering
with Specialization in Energetic Systems

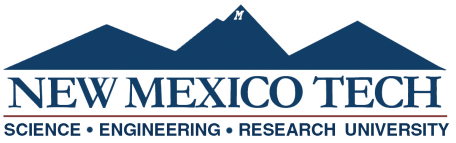

New Mexico Institute of Mining and Technology
Socorro, New Mexico
May, 2025

This thesis is dedicated to my loved ones who stuck with me during my journey and to my loved ones who have passed on. Without your support, I wouldn't have made it through the various seasons of life.

Autumn Noël Weber
New Mexico Institute of Mining and Technology
May, 2025

ACKNOWLEDGMENTS

I would first like to thank my research advisor, Dr. Michael Hargather, for his support over the past two years. I would not have been able to move on in my career and determine what I wanted to do without his guidance. I would also like to thank Dr. Frank Austin Mier for stepping into the role of director for the lab group and mentoring me over the last year. Without his willingness to jump in, I would not have been as successful in finishing my degree. I want to thank Dr. Daniel Jones for mentoring me through the "squishier" parts of science and allowing me to pretend to be a caver, even if just for one weekend.

Thank you to my parents, Brian and Grace, for supporting me through this crazy dream and never giving up on me, even when I gave up on myself. Thank you for fostering my curiosity about God's creation, even when it scared you. Momma, thanks for talking me back into my wild ideas when the world got to me, even if it was telling me I could let spite win this one time. Daddy, thank you for giving me my love for science and nature. All I ever wanted was to be like you, and without that, I wouldn't be here.

To my little sister Trysten, thank you for being the best partner in crime and my constant inspiration. To my grandparents, your sacrifices made this possible. It's an honor to carry your legacy. To my best friends Kim, Hailey, Lucia, Victoria, Maria, and Jessie, thank you for the late-night talks, rants, ice cream runs, and encouragement.

Chris, thank you for being my rock through this process and reminding me to drink water. To the rest of my family, both biological and chosen, thank you for listening to my endless ramblings about God, science, and life. Your love and prayers gave me strength.

To both the SGDL and the EFDL, thank you for the lab lunches and science shenanigans. I will always cherish the memories made during our time together.

This research was supported by NASA Grant 80NSSC23K0641 with PI Dr. Daniel Jones at New Mexico Tech.

This thesis was typeset with LaTeX[1] by the author.

[1]The LaTeX document preparation system was developed by Leslie Lamport as a special version of Donald Knuth's TeX program for computer typesetting. TeX is a trademark of the American Mathematical Society. The LaTeX macro package for the New Mexico Institute of Mining and Technology thesis format was written by John W. Shipman.

ABSTRACT

Particles are released and deposited behind objects as they move through an environment due to their trailing wake. These deposited particles create contamination fields in the environment. Mapping this contamination spread behind walking people provides a way to understand and characterize human impact on a notional pristine environment like an alien planet. Small-scale testing utilized an airbrush as a notional contamination source to emit paint droplets, which settled onto the surface below in a characteristic pattern. The paint deposition pattern under different experimental conditions was analyzed using image processing to create concentration graphs. These graphs were nondimensionalized leveraging key nondimensional numbers identified with a Buckingham Pi analysis. Full-scale experiments utilized human subjects walking through a controlled environment to measure wake parameters and deposition of contaminants. Jet and human aerodynamic wake scaling techniques were used in tandem with Reynolds analogy to demonstrate the similarity between the two experimental systems. This similarity yielded an experimentally-informed, scalable preliminary model that maps the particle settling from trailing wakes nondimensionally.

Keywords: Planetary protection; Buckingham Pi scaling; Jet scaling; Reynolds analogy; Nondimensionalization

CONTENTS

LIST OF TABLES

LIST OF FIGURES

Figure **Page**

LIST OF ABBREVIATIONS

ρ_p	Density of the particle
ρ_f	Density of the fluid
u	Fluid velocity
g	Gravity
t	Time
μ_f	Viscosity
d_p	Particle diameter
l	Test section length
d_n	Characteristic length
w	Test section width
h	Height
I	Pixel intensity
s_0	Virtual origin
s	Streamwise coordinate
r	Spanwise coordinate
Stk	Stokes number
Fr	Froude number
Eu	Euler number
Re	Reynolds number
SPME	Soild-phase microextraction
GC-MS	Gas chromatography mass spectrometer
NVR	Nonvolatile residue
RTT	Reynolds Transport Theorem
SPME	Solid phase microextraction

This thesis is accepted on behalf of the faculty of the Institute by the following committee:

Michael J. Hargather

Academic and Research Advisor

Frank Austin Mier

Daniel S. Jones

I release this document to the New Mexico Institute of Mining and Technology.

Autumn Noël Weber July 2, 2025

CHAPTER 1

INTRODUCTION

1.1 Research Motivation

A challenge for planetary exploration is the potential contamination of alien worlds due to human presence during exploration [1]. Previous research has explored determining how organisms are dispersed across the globe. However, little research has been performed on determining the spread in extraterrestrial environments [2, 3]. Humans are constant sources of contamination because our bodies continuously shed skin cells [4]. These can be entrained in the human thermal plume [5] or wake if a person is moving [6]. Additionally, chemical or biological materials from bodies, including residues from personal care products, are dispersed similarly as contaminants [7]. This contamination is ultimately deposited onto the surface behind people, creating a contamination field as they move. Even equipment built in clean room environments on Earth, such as rovers, can be contaminated with these particles [8, 9]. The introduction of otherworldly contamination presents a challenge in determining whether the biological materials found are native or not, a point that was identified by Race et al. 2015 [10]. Therefore, methods to mitigate, manage, and track this passive scalar contamination spread are of high interest.

1.2 Literature Review

1.2.1 Scalar contamination deposition in extraterrestrial exploration

The deposition of scalar contamination in the aerodynamic wake of a moving object is of particular concern for planetary exploration, where even trace levels of biological or chemical material can compromise scientific findings [1]. The term passive scalar contaminant describes that the contaminant is not self propelled and has no direction. While terrestrial studies have characterized the dispersion of microbial and chemical contaminants, relatively little research has addressed how these processes manifest in extraterrestrial environments [2, 3]. The reduced gravity, lower atmospheric pressure, and differing flow regimes on

bodies such as Mars may significantly alter the behavior of contaminant transport and deposition. Furthermore, even equipment constructed in cleanroom environments, such as planetary landers and rovers, has been shown to retain trace contaminants despite rigorous decontamination protocols [8, 9]. The presence of these materials complicates efforts to distinguish between native and introduced biological signatures, a concern emphasized by Race et al. [10]. Understanding and modeling scalar contamination in non-Earth environments is, therefore, essential to developing mitigation strategies and preserving the scientific validity of planetary exploration missions.

1.2.2 Nondimensionalization - Buckingham Pi Theorem

The foundation of modern dimensional analysis was established by Buckingham in 1914 through his development of the Buckingham Pi theorem [11]. His theorem provided an approach to identifying fundamental dimensionless parameters that govern physical systems, allowing for the reduction of complex equations to more manageable forms. This methodology allows for the comparison of phenomena across different physical scales by ensuring similarity through nondimensional groupings. Through this framework, small-scale laboratory experiments can be effectively scaled to predict the behavior of full-scale systems. Classic dimensionless numbers, such as the Reynolds number [12], which characterizes inertial to viscous forces in fluid flow, and the Froude number [13], which compares inertial to gravitational forces, are direct outcomes of this theorem. The utility of this approach extends far beyond fluid mechanics, having been adopted to model complex and multiphysics systems across disciplines, including thermal-fluid systems, aerodynamics, and biochemical processes [14, 15] to understand the connection of different variables and how they affect the physics of the system.

1.2.3 Human thermal plume and human aerodynamic wake

As a person stands in an environment, thermal energy is continuously exchanged between the body and its surroundings. Computational fluid dynamics (CFD) simulations and experiments conducted by Craven et al. [5] demonstrated that the convective nature of the human thermal plume (HTP) induces air movement and facilitates contaminant transport into the surrounding environment. Once a person moves, the HTP becomes a phenomenon known as the human aerodynamic wake (HAW). CFD simulations of the HAW demonstrated where each of the different flow regions occurs in the HAW and where the scalar contaminants are concentrated within these different regimes [6, 16, 17]. In an additional study by Edge [18], a characteristic length and ideal walking speed were identified for wake transport. The contamination concentration regions and flow regimes were nondimensionalized based on the characteristic length, which was

identified to be the width of the shoulders of the person. Studies were conducted to find the point of transition between HTP and HAW, as well as to define the role of wake turbulence and body movement in scalar contaminant transport and dispersion [19]. Additionally, studies explored how to leverage this contamination transport in the HAW. Based on these findings, Volpe [20] was able to leverage the passive transport of scalar contaminants in an HAW to detect chemicals found on a person. The Aerodynamic Wake Sampling Portal leverages natural airflow patterns behind walking individuals to enable rapid, high-throughput chemical trace detection.

1.2.4 Mixing, jets, and dispersion

Mixing and dispersion studies have been performed on both large and small scales. Wygnanski and Fiedler [21] studied turbulent, two-dimensional, axisymmetric jets and discovered that the jet demonstrates self-similar behavior. The study also delved into the turbulence statistics and how more efficient mixing leads to more contamination spread. Spray deposition from different nozzles has been explored in the literature. Work by Kluza et al. [22] was done to predict the uniform spray coverage of various types of flat fan nozzles to determine a mathematical model.

Expansion on contaminant mixing was done on the human scale. The influence of human-induced wake flow on indoor air dynamics and particle dispersion has been explored by Tao et al. [23], which demonstrated that walking speed plays a critical role in exposure to a contaminant, as faster speed lowers the risk. Faster movement enhances ventilation and reduces particle retention, while slower movement allows contaminants to accumulate. Investigation of wake collection and plume transport by Smith [24] confirms that the wake region of a blunt body object serves as a natural collector of airborne contaminants. Experimental results validated the effectiveness of wake-based sampling [25]. Modeling of the exhaust deposition behind a vehicle was done by Samson [26]. Due to the nature of vehicle exhaust, this study was not steady state, which caused limitations.

1.2.5 SPME and other methods for organic contaminant detection

Solid-phase microextraction (SPME) was developed in 1989 by Pawliszyn [27]. SPME is an analytical chemistry technique in which a thin wire, fiber, or arrow, which is a thin stainless steel wire, is coated with a sorbent. This sorbent coating is a material that readily absorbs chemical vapors released into the air that can be analyzed in a variety of ways. Reviews of SPME were done by Sajid et al. in 2018 [28] and Jalili et al. in 2020 [29]. These reviews highlighted several advantages of SPME, including that it is solvent-free, allows for reduced processing time, and can integrate into various instruments. The review also highlighted

the drawbacks of the technique, such as being one-time use, difficult to transport, and not having the same quantification power in comparison to other methods. There are various SPME configurations for different applications. SPME fiber consists of a thin fiber that is protected by a hollow needle when it is not exposed to the environment. This is the most popular design in the SPME family. SPME arrows were designed to handle a larger amount of SPME sorbent volumes and are ideal for GC analysis. Some challenges for this analysis technique are how delicate they are, the high purchase cost, and the limited amount of sorbent. A review of SPME arrows was further done by Herrington et al., and reinforced this idea that SPME arrows are an improvement on SPME fibers [30].

Methods for extracting volatile organics in the air can be done using SPME fibers and arrows. Prosen reviewed this extraction technique and its effectiveness in 1999 [31]. In the paper, the theory, factors of performance, limitations, and applications were explored, and it was concluded that SPME was a simple and relatively low-cost analysis method. Headspace solid-phase microextraction (HE-SPME) is a solvent-free sample preparation technique for analyzing volatile compounds. Zhang and Pawliszyn in 1993 [32] found that this technique was good for analyzing complex or solid matrices, with a matrix referring to an array of analytes, including the analyte of interest. This method induced less contamination during analysis due to the simplicity of the analysis.

SPME is often coupled with gas chromatography-mass - mass spectrometry (GC-MS), an analytical method developed by Gohlke and McLafferty in 1959 [33]. This analysis method enables precise identification and quantification of compounds extracted by SPME techniques. Kitson's 1996 textbook [34] outlines the methodology for quantitative GC-MS.

In addition to SPME wires, more passive chemical collection methods exist for contamination monitoring. One such method was developed by Borson et al., who introduced a standardized approach for quantifying nonvolatile residue (NVR) contamination [35]. This technique was later formalized as ASTM Standard E1235. It involves placing a witness foil, a specially prepared foil surface, in an area of interest, where it passively collects airborne or contact transferred residues. After exposure, the collected contaminants are gravimetrically quantified by dissolving them in a solvent and measuring the solid material left behind after evaporation.

In this context, NVR refers to the solid deposits that remain after a volatile solvent has evaporated. When applied to witness foils, NVR serves as an important metric of surface cleanliness, especially in contamination-sensitive environments such as cleanrooms, aerospace assemblies, and electronics manufacturing. The presence of NVR can interfere with equipment performance, reduce material reliability, and compromise mission success. As such, NVR testing is routinely conducted to verify cleanliness standards and mitigate the risk of contamination-related failures.

1.3 Objectives for Present Research

The present work will focus on determining the factors that affect the particle settling from trailing wakes behind theoretically representative geometries, characterizing the contamination spread. To determine this, this research determines the statistical trends of the contamination settling pattern and the environmental factors that affect the contamination settling pattern.

The research here will:

- Determine the statistical settling pattern on a horizontal surface of the paint deposition created by a paint spray jet
- Develop a nondimensionalization technique of the spray deposition
- Explore the scalability between a person walking through a fluid system in a quiescent atmosphere and a spray deposition

CHAPTER 2

NONDIMENSIONALIZATION USING BUCKINGHAM PI THEOREM

The methodology and evolution of the nondimensionalization used to create a scalable model are discussed. The end relationship relates the Stokes number, the density ratio between the particle and the moving fluid, the Froude number, the Reynolds number, the length ratio between the characteristic length and the particle diameter, and the length ratio between the characteristic length and the height of the source. This relationship helps define the relationships between the different parameters and how they apply to physics.

2.1 Methodology

Table 2.1: Identification of the quantities used in the Buckingham Pi analysis

Variable	Value	Units
u_f		m/s
d_n		L
ρ_f	fluid density	M/L^3
ρ_p	particle density	M/L^3
g	9.81	m/s^2
μ_f	fluid dynamic viscosity	L^2/T
d_p	particle diameter	L

Dimensional analysis creates relationships between different terms in a complex system. Buckingham [11] developed a method that allowed for complex systems to be defined by a small group of nondimensional parameters called Π groups. This method helps identify and relate known nondimensional numbers for complex flow systems that are not completely bounded by known equations. This is done by first identifying the independent and dependent variables for a system. This method is helpful in scaling between systems due to its ability to create relationships, which allows for scaling. Two systems are physically similar if the Π terms are the same between them.

The Π numbers that define a system were identified based on the number of variables involved in the relationship, as listed in Table 2.1. It is important to note that t is the relaxation time or the time it takes for a particle to fall. These variables were used to construct the dimensionless Π numbers, which characterize the system's behavior. The total number of Π numbers is determined by subtracting the number of repeating variables (3) from the total number of variables (9), resulting in (6) independent dimensionless products. There are two methods for determining r. The first method involves calculating the rank of the dimensional matrix, which is found by selecting the largest square submatrix with a nonzero determinant. The second method is based on identifying the number of fundamental dimensions in the system from the dimensional matrix. This dimensional matrix for both these methods is shown below.

Table 2.2: Identified variables of interest and their associated dimensions

	u_f	d_n	h	ρ_f	ρ_p	g	μ_f	d_p	t
Mass (M)	0	0	0	1	1	0	1	0	0
Time (T)	-1	0	0	0	0	-2	-1	0	1
Length (L)	1	1	1	-3	-3	1	1	1	0

To construct the Π numbers, r number of repeating variables are selected. The repeating variables must have different dimensions and must contain all of the fundamental dimensions in combination with each other. The parameters are typically chosen to fill three requirements: one is a characteristic velocity, one is a characteristic length, and one is a fluid property. It is important to note that humidity is neglected in this dimensional analysis and throughout this thesis due to the complexity that this variable introduces.

2.2 Relationship development

The experiments that were nondimensionalized are a person walking through a system with a trailing aerodynamic wake behind them and a jet spraying above a horizontal surface, both shown in Figure 2.1. These figures show where the different variables of interest are in each experiment. Both of these experiments were considered due to a jet being a simpler experiment to conduct. The nondimensionalization allows for investigation into whether or not a jet is a justifiable small-scale alternative to a person walking through a system.

As shown in Table 2.1 and Figure 2.1, the nondimensionalization process began by identifying the key variables in the system and constructing a dimensional matrix based on their fundamental dimensions: mass (M), length (L), and time (T). The matrix was found to have a rank of three, indicating that three repeating variables were needed. The variables u_f, d_n, and ρ_f were chosen as the repeating variables since they satisfy the necessary criteria. These repeating variables were

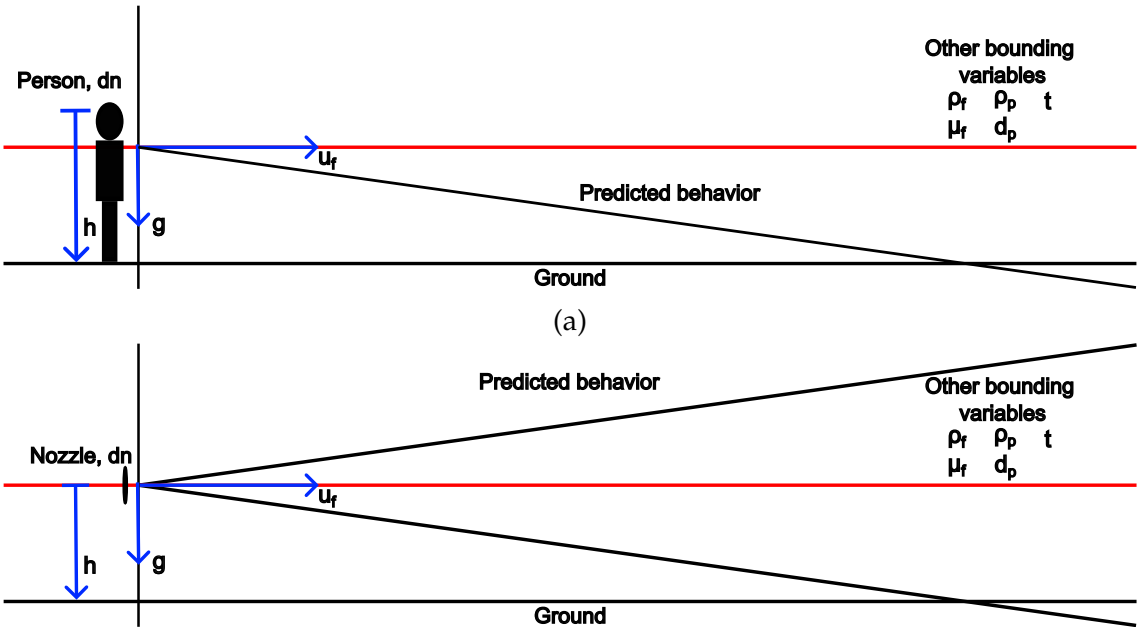

Figure 2.1: a) Diagram of predicted behavior with selected variables, where d_n is the shoulder width, h is the height of the person, g is gravity, u_f is velocity of the person walking, ρ_f is the density of the fluid, μ_f is the dynamic viscosity of the fluid, ρ_p is the density of the particle, d_p is the diameter of the particle, and t is relaxation time. b) Diagram of predicted behavior with selected variables, where d_n is the nozzle diameter, h is the height of the nozzle, g is gravity, u_f is velocity of the fluid, ρ_f is the density of the fluid, μ_f is the dynamic viscosity of the fluid, ρ_p is the density of the particle, d_p is the diameter of the particle, and t is relaxation time.

then used to form dimensionless groups by combining them with the remaining variables in the system. The initial relationship between the variables before applying Buckingham Pi is expressed in equation 2.1:

$$u_f = f(t, d_n, h, \rho_f, \rho_p, g, \mu_f, d_p) \tag{2.1}$$

The system under analysis consists of nine variables and is described using three fundamental dimensions: mass, time, and length. Based on this information, the number of resulting Π numbers was calculated to be five using both the dimension-counting method and the matrix rank method. For the selection of repeating variables, u_f was chosen to represent a characteristic velocity, d_n as the characteristic length scale, and ρ_f to represent a fluid property.

After applying the Buckingham Pi Theorem, a set of dimensionless numbers was derived. These include Stokes number (Stk), Froude number (Fr), Reynolds

Table 2.3: Π numbers chosen using Buckingham Π analysis

Π number	Π group	Nondimensional number	Relationship
Π_1	$\frac{\rho_p d_p^2 u_f}{18 \mu_f d_n}$	Stokes number	$\frac{\text{Particle relaxation time}}{\text{Characteristic flow time}}$
Π_2	$\frac{\rho_p}{\rho_f}$	-	Density ratio
Π_3	$\frac{u_f}{\sqrt{g d_n}}$	Froude number	$\frac{\text{Inertial force}}{\text{Gravitational force}}$
Π_4	$\frac{u_f d_n \rho_f}{\mu_f}$	Reynolds number	$\frac{\text{Inertial force}}{\text{Viscous force}}$
Π_5	$\frac{d_p}{d_n}$	-	Length ratio
Π_6	$\frac{h}{d_n}$	-	Length ratio

number (Re), as well as three ratios. One is a ratio between the fluid density and particle density, and the other two are length ratios: one between the characteristic length and the particle diameter, and one between the characteristic length and the height. All of these nondimensional numbers are shown in Table 2.3. In this nondimensionalization, relaxation time is converted into $\frac{\rho_p d_p^2}{18 \mu_f}$ since this combination of parameters describes relaxation time. Each of these dimensionless numbers serves a specific role in characterizing the system's behavior. The Stokes number describes the response of particles within a fluid flow, particularly how they follow the motion of the surrounding fluid. The Froude number is used to distinguish between different flow regimes. The Reynolds number is a widely used indicator of fluid flow behavior, predicting whether the flow will be laminar or turbulent. The finalized, nondimensional form of the relationship is then written in terms of these Π groups.

$$Stk = f(\frac{\rho_p}{\rho_f}, Fr, Re, \frac{d_p}{d_n}, \frac{h}{d_n}) \tag{2.2}$$

Stokes number, as shown in Table 2.3, is the ratio between particle relaxation time and characteristic flow time. Particle relaxation time is the decay of its velocity due to drag, and the characteristic flow time is the time it takes for a fluid to move through a system or to reach a specific state. A particle with a small Stokes number follows the flow streamlines, whereas a particle with a larger Stokes number has inertia dominating its motion and will continue on its initial path. The final version of the Stokes number presented uses the Stokes flow or creeping flow solution for the particle relaxation time. This solution describes the fluid flow where the inertial forces are small in comparison to the viscous forces in the system. This solution also assumes flow over symmetric geometries, like spheres.

2.3 Experimental values

Table 2.4 shows the of values for the different variables considered in this analysis.

Table 2.4: Identification of the quantities used in the Buckingham Pi analysis

Symbol	Quantity description	Quantity
u_f	paint fluid velocity	10 m/s
ρ_f	air density	1.2 kg/m^2
μ_f	air dynamic viscosity	$1.5 * 10^{-5}$ m^2/s
μ_f	paint dynamic viscosity	350 m^2/s
g	gravity	9.81 m/s^2
u_f	wake fluid velocity	1.34 m/s

Average velocity measurements were obtained by compiling and averaging multiple anemometer readings taken from the exit of the airbrush to reduce random error and in an attempt to capture representative flow conditions. The fluid density, ρ_f, and dynamic viscosity, μ_f, were taken from the property data reported by Petrosyan et al. [36], which provides experimentally validated values for the Earth for comparison to Mars, which was one of the goals of this research. Paint dynamic viscosity was determined by online product sheets obtained. Wake fluid velocity was determined from the literature [6].

2.4 Reynolds transport theorem

In fluid dynamics, the principles of conservation of mass, momentum, and energy form the foundation for deriving equations that describe the behavior of a fluid system. Each of these conservation equations involves a diffusive coefficient and the rate of change of a particular property. According to the Reynolds Transport Theorem (RTT) [37], the dimensional similarity among these equations allows for relationships to be established between them.

RTT is particularly useful because it enables the estimation of the diffusivity of one property based on the known behavior of others. This is especially helpful in cases where direct measurement is challenging, such as in mass transfer.

Fundamentally, RTT connects the rate of change of a property within a control volume to the flux of that property across its boundaries. It serves as a bridge between the concepts of a control mass and a control volume. A comparison of these properties for the different conservation laws is shown in Table 2.5.

Table 2.5: Quantity comparison between mass, momentum, and energy conservation

Entity	Rate of change	Diffusion coefficient	Coefficient units
Mass	$\frac{d}{dz}(C_a)$	Binary diffusion coeff., D_{aj}	$\frac{length^2}{time}$
Momentum	$\frac{d}{dz}(\rho v)$	Kinematic viscosity, ν	$\frac{length^2}{time}$
Energy	$\frac{d}{dz}(\rho C_p T)$	Thermal diffusivity, κ	$\frac{length^2}{time}$

2.5 Reynolds analogy

Reynolds analogy is a framework that links momentum, heat, and mass transport within a fluid system [38]. This analogy comes from the observation that the equations that govern the different transport processes are similar. This analogy becomes particularly useful in turbulent transport due to it being easier to measure turbulent momentum transfer in comparison to turbulent mass transfer.

Reynolds analogy suggests that the turbulent diffusivity of momentum can be related to the turbulent diffusivity of heat or mass. This leads to simplified expressions, such as equating the Stanton number, a nondimensional number used to quantify the ratio of heat transfer to the thermal capacity of a fluid, to half the skin friction coefficient under certain conditions. Such relationships eliminate the need for separate detailed models of heat and mass transfer, provided the velocity field is known.

The usefulness of Reynolds analogy lies in its ability to predict heat or mass transfer from fluid flow characteristics alone. This analogy becomes particularly useful in turbulent transport due to it being easier to measure turbulent momentum transfer in comparison to turbulent mass transfer. However, the classical form of Reynolds analogy assumes constant fluid properties and negligible pressure gradients, which limits its applicability, specifically when the system's Prandtl number is greater than one. The Prandtl number is the ratio of momentum diffusivity to thermal diffusivity.

The key distinction between RTT and Reynolds analogy lies in what they relate to. RTT provides a generalized conservation framework applicable to any scalar or vector property in a transport system, while Reynolds analogy draws equivalencies between specific transport processes under simplified assumptions. Reynolds analogy is an approximation, best suited to turbulent flows and engineering estimations.

2.6 Earth compared to other environments

Each planet exhibits a distinct set of environmental conditions, including differences in gravity, temperature ranges, and atmospheric chemistry. On Earth, these variables support a well-understood set of physical, chemical, and biological processes. However, on Mars, for example, gravity is only about 38% of Earth's, the atmospheric pressure is less than 1% of Earth's, and the atmosphere is composed primarily of carbon dioxide with very little oxygen or nitrogen. Additionally, Martian surface temperatures can drop to below -100°C. Table 2.6 compares values for air density, kinematic viscosity, and gravity between Earth and Mars to provide a comparison for the phenomena explained above. These values were pulled from Petrosyan et al. [36] since this paper compares the values between the two planets.

Table 2.6: Earth versus Martian environmental properties

Property	Earth	Mars	Units
Air density, ρ	1.2	0.015	kg/m^3
Dynamic viscosity, μ	1.5×10^{-5}	1×10^{-3}	m^2/s
Gravity, g	9.8	3.7	m/s^2

Because of these differences, experimental results obtained on Earth, where conditions are relatively stable, may not accurately predict how systems will behave on Mars. This is especially critical in areas such as fluid dynamics, microbial survival, and equipment performance. Therefore, when designing experimental systems intended for Mars, it is important to determine how the system scales between Earth and Mars. Buckingham Pi Theorem can provide the groundwork to scale between the different atmospheric conditions.

CHAPTER 3

EXPERIMENTAL METHODS FOR THE PAINT JET EXPERIMENT

Small-scale experiments allow for control over environmental conditions that influence the characteristic deposition of a passive scalar contaminant. This allows for determining which environmental conditions influence the deposition pattern more. Here, a paint airbrush sprayer is used as a "contamination" source for the paint droplets. Statistical analysis of the deposition was done for each experimental case.

3.1 Justification for using a paint jet

To study the deposition behind a moving person, a small-scale, simplified experiment was needed. Going off the work of Edge et al. [6], it is known that the wake of a person scales with the width of the shoulders. Therefore, a simplified experiment allowing this relationship to be leveraged was important. As discussed in Chapter 2, the Buckingham Pi Theorem creates relationships that allow for scaling between related scenarios. Additionally, jet scaling laws are well-defined in the literature and are commonly used [39]. Due to this, using the known jet scaling laws in tandem with the Buckingham Pi Theorem allowed for the development of a small-scale test that could isolate the experiment from the surrounding environment and control different input parameters. As shown schematically in Figure 3.1, an assumption is made that the human form acts as the airbrush nozzle, depositing contamination in the wake and onto the ground in the same characteristic pattern as these airbrush experiments. Jet behavior and particle deposition were used to model the contamination spread in the wake of a moving person. A change in reference frame is needed to change between the spray jet and a person moving through an environment. A person walks through still air, however, if the reference frame is changed to the person is fixed and the surrounding environment is moving, this arrangement matches a spray jet.

3.2 Box design

The paint jet experiment was performed inside a box made with 0.64 cm thick acrylic sheets and 2.54 cm by 2.54 cm 80/20-compatible t-slotted framing

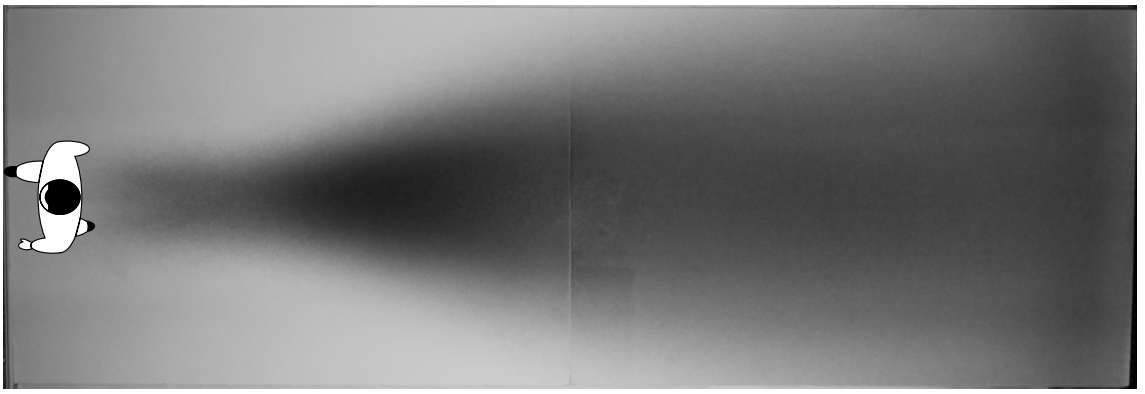

Figure 3.1: Diagram of how a trailing wake relates to a paint-filled jet

bars to isolate the test area from any surrounding cross flow. A 0.64 cm thick aluminum honeycomb was used on the front and back of the box to allow airflow to be parallel with the paint jet. Due to the expansion of the paint jet as it exited the airbrush, the box was open to the air on the top to prevent the paint from sticking to the acrylic and distorting the imaging area. Figure 3.2 shows images of the final box design, and Table 3.1 presents the dimensions.

Table 3.1: Experimental spray box dimensions

External width, x cm	External length, y cm	External height, z cm	Dist to camera cm
61.0	152	61.0	147

3.3 Experimental setup

A 151.5 cm by 59.5 cm piece of white foam core was laid on the bottom of the box for each spray test. This was selected as the medium to collect the paint deposition to prevent warping in the areas of high paint deposition and to create a uniform background.

An Iwata-Medea Studio Series Power Jet Lite Double Piston Air Compressor was used to provide air for airbrush operation. Additionally, an Iwata-Medea Revolution HP SAR Single Action Bottle Feed with an exit nozzle diameter of 6.75 mm was used to disperse the paint, which is shown in Figure 3.3. During experiments, it was held by a person to push the button on the airbrush. The amount of paint added into the air jet was controlled by a 3D printed clip that was 2.9 mm thick made sure that the same amount of paint was added into the spray every time, which is shown in Figure 3.3b and 3.3c. With this constant paint inclusion, the amount of time each experiment took to ensure constant paint

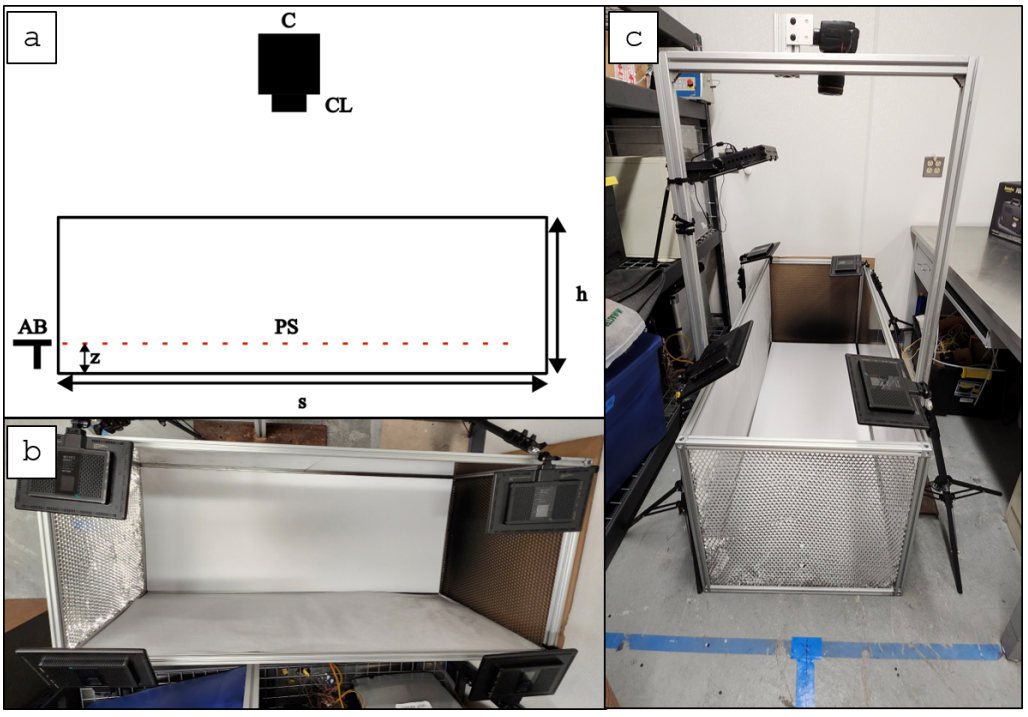

Figure 3.2: a) Diagram of the spray box, where AB is the airbrush, PS is the paint stream, C is the camera, CL is the camera lens, z is the height of the airbrush, s is the length of the box, and h is the height of the box. b) Picture of the spray box from above the experimental spray box. c) Picture of the experimental spray box from the right side of the box.

mixing was about 235 seconds. Createx airbrush colors opaque paint in the color black was used in all experiments to maintain consistency in the paint properties throughout.

A Nikon D780 DSLR camera with an AF-S Nikkor 24-120 mm lens was used to capture images during the test. These images capture the temporal evolution of the paint deposition throughout the experiment. The camera was mounted on a frame made out of 7.62 cm by 7.62 cm 80/20-compatible t-slotted framing that was suspended above the box floor so that the distance from the camera lens to the box floor was 147 cm. The lens was set to 28 mm, and one picture was taken every second during the experiment. An additional five images were recorded before the experimental background pictures, before the paint jet started depositing paint. Figure 3.2c shows the camera mounted above the spray box.

Three different paint airbrush setups were studied and are shown in Table 3.2.

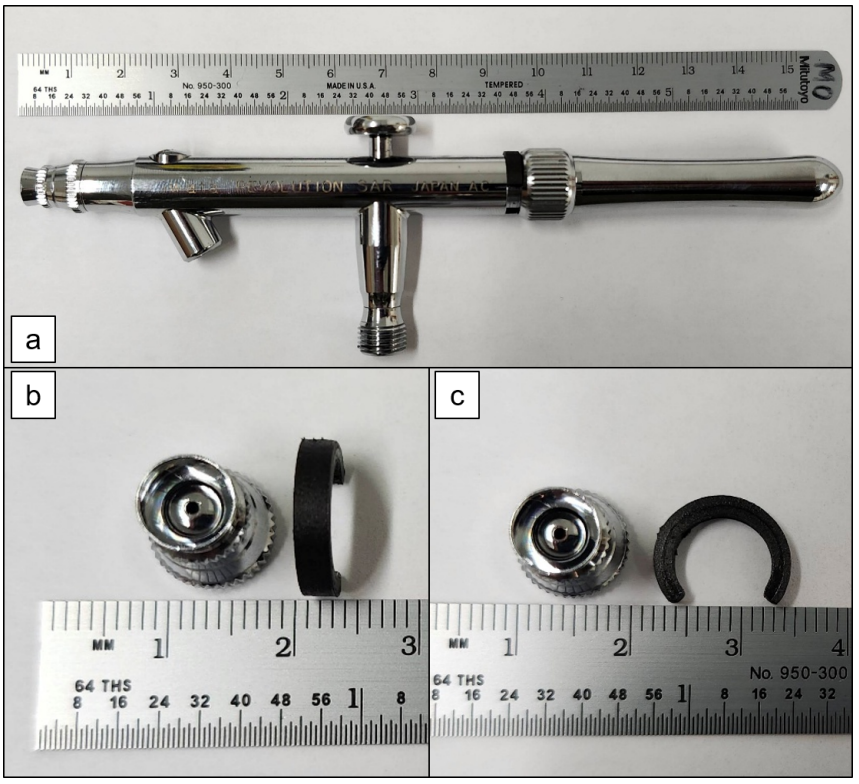

Figure 3.3: a) Picture of the fully assembled airbrush with nozzle and 3D printed clip for consistent paint inclusion. b) Picture with an airbrush nozzle and a 3D printed clip head on. c) Picture with an airbrush nozzle and a 3D printed clip on the face.

3.4 Image processing

Image processing routines were used to quantify the concentration of the paint deposited onto the white surface at the bottom of the test section. The process starts with selecting the final and initial background images for each experiment. Both images were cropped to the experimental area so that all processing was done in the experimental area alone. Additionally, images were corrected for any camera misalignment from the experiment, such as small angle rotations. To process the picture sets, each image was first converted from color to grayscale, allowing the pixel intensities to be a value between 0 and 255, with 0 relating to pure black and 255 relating to pure white. After this conversion was completed, the initial background image was subtracted from the final image. This was done so that any background noise in the form of shadows and abnormalities in the foam core was removed from the analyzed image. A small amount of pixel intensity shift was added so that the subtracted image features were more visible for visualization. Once this was done, the intensity of the background was found for each image set.

Table 3.2: Different airbrush configurations

	Pressure kPa	x_o cm	Nozzle height, z cm	Paint inclusion mm
Case 1	400	32.5	12.07	2.6
Case 2	400	32.5	21.87	2.6
Case 2	400	32.5	28.35	2.6

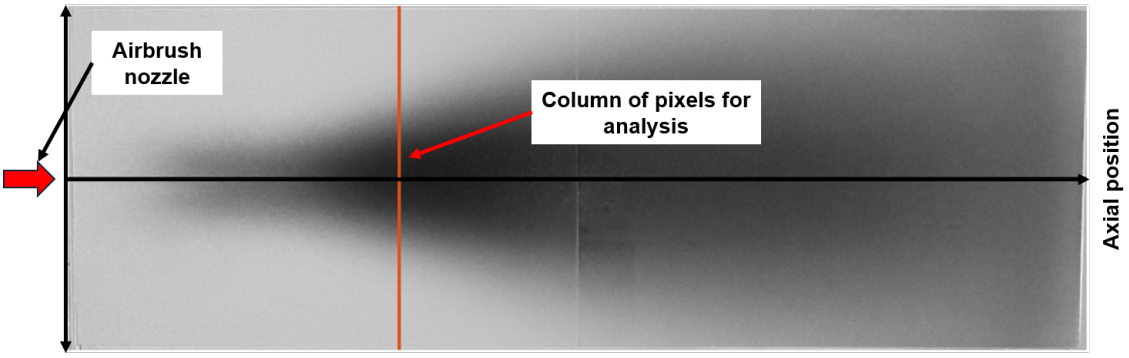

Figure 3.4: Analyzed picture with a column of pixels for analysis highlighted.

Physical dimensions were converted to the pixel length using known lengths shown in the picture as reference lengths for conversion. Next, length, now referenced as the downstream position, was nondimensionalized with the exit nozzle diameter of the airbrush. The MATLAB code created for this analysis drew a line in the downstream direction to mark the center axis of the exit nozzle to allow for visual verification that the center line was properly identified. This identified center line was used later to correct the data. Then, analysis lines were drawn on the image. An example of this is shown in Figure 3.4. The analysis lines were initially spaced by 15 diameters starting from the spray origin and going downstream. The pixel intensity values for each column were collected and stored in an array where each of the analysis lines was drawn. Once all these arrays were collected, the processing adjusted the data for plotting.

With each column of pixels, a three-column vector of data was created. One column corresponds to the pixel intensity values, one column corresponds to the x-coordinates of the pixels, and the last one corresponds to the y-coordinates of the pixels. Since 0 correlates to the color black and 255 correlates to the color white, the inverse of intensity is proportional to the paint concentration in each picture. The pixel intensity values are inverted to reflect this idea. Due to lighting, the foam core background does not appear completely white in the greyscale images. To account for this, the pixel intensity of the foam core was found and subtracted from the inverted pixel intensities. These transformed intensities now represent contamination concentration. The size of the y-coordinate array was found to determine the center. With this, the center line correction value found in

the previous discussion was used to adjust the center line of the vector. Next, the y-coordinate array was nondimensionalized with the diameter of the exit nozzle so that it matched the nondimensionalization done previously. This process was repeated until all analysis lines were converted to contamination and nondimensionalized axial position vector pairs.

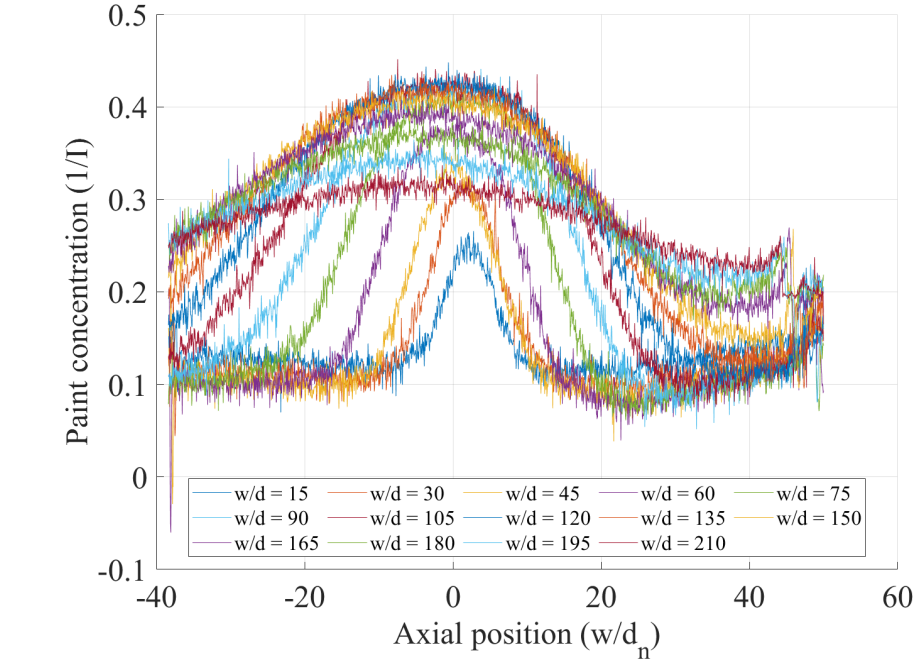

(a)

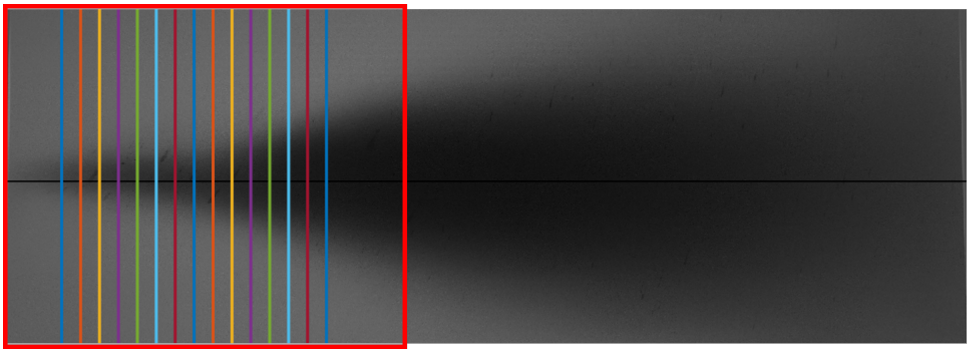

(b)

Figure 3.5: a) Plot of inverted pixel intensities versus nozzle diameter normalized axial position at different downstream positions, which are also nozzle diameter normalized. b) Vertical lines at the different downstream positions within the area of interest, which is surrounded by a red box.

The area of interest was determined based on the settling pattern observed in the images. Since these experiments were conducted inside a closed environment to isolate the event from the surrounding environment, the edges of the

box created regions where boundary conditions must be considered. These regions of interest were determined based on the concentration curves. Looking at a two-dimensional plot of the intensities shown in Figure 3.5a, collapsing-like behavior can be seen in diameters 120 through 240. This was most likely because the paint particles in the spray jet are being constrained into a smaller region than they would be if the wall were not there. Centerline drift occurs as the distance downstream is increased, which is especially shown in diameters 120 to 240. To analyze this further, the spacing between analyzed columns was decreased to 5 diameters, where further collapsing behavior was seen, which is shown in Figure 3.5b. By exclusively analyzing the identified area of interest, the paint concentration curves show similar Gaussian distribution behavior. This is shown in Figure 5.1

3.5 Paint droplet characterization

Paint particle size analysis was performed to characterize the particle size distribution throughout the deposition field. Testing locations were set up at 10-diameter intervals starting at 15 diameters downstream and ending at 95 diameters downstream, which is shown in Figure 3.6. An additional testing location on each side of the centerline were also set up next to catch the spray deposition spread in the axial direction for locations 55 through 95, The overall region was selected due to this being inside the area of interest identified during the paint jet experiment image processing. Glass slides to collect paint particles were placed at each testing location to collect the paint as it was deposited by the paint jet. Figure 3.6 shows the downstream positions where the glass slides were placed about the jet origin. These placements were found by placing the glass slides on a previously done spray deposition and using it to determine where slides could be placed for optimal characterization. Four different test cases were analyzed: A burst paint test, a 1 second paint test, a 3 second paint test, and a 5 second paint test. These intervals were selected so that the glass slides would not be so over-saturated with paint that paint droplet sizing could not be done.

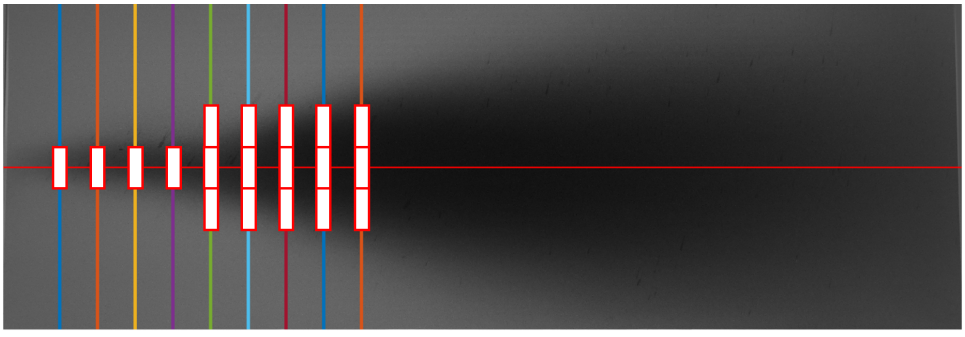

Figure 3.6: Starting from the left at 15 diameters, testing location lines increase by 10 diameters downstream.

To analyze the glass slides, pictures were taken at different locations on the slide with an AmScope ME 580 series compact trinocular metallurgical compound microscope. These were used to find the average size of the paint particles. One set of pictures was taken at the center of the glass slides, aligned with the spray's center, and another set of pictures was taken in the axial direction. Figure 3.7 shows an example of one of these images.

Image processing techniques were used to identify the size of the paint droplets. First, a local Laplacian filter was applied to each image. This enhances the edges for easier detection. The images were converted to grayscale before binarization. With each of the images now in black and white, the colors were inverted so that black pixels became white and vice versa. Any white regions, which represent paint droplets, were filled. Morphological operations of erosion and dilation were used to remove noise in the images. If any white regions in the image were connected, they became one area to be measured. The area of each white region was then found if the region was determined to be 75% circular. From this area, the diameter of the assumed circular droplet was determined. For each test condition and location, the average diameter of the paint droplets was calculated, in addition to sizing the particles for statistical analysis.

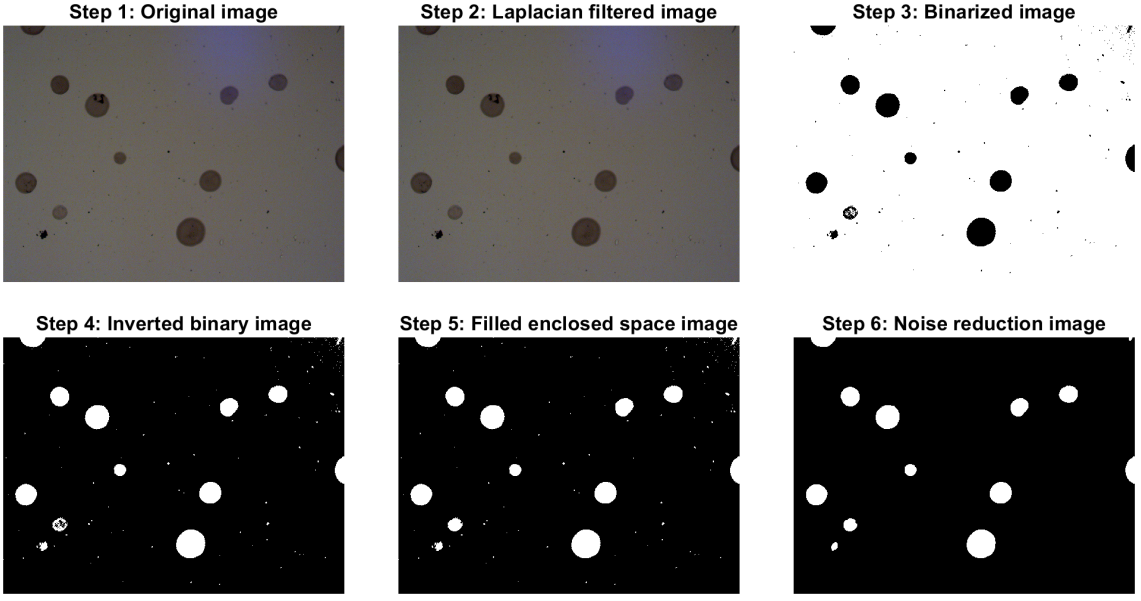

Figure 3.7: Step 1: Original image taken of the glass slide with the microscope. Step 2: Laplacian filtered the image to enhance the edges. Step 3: Binarization of the image. Step 4: Inversion of the binary image. Step 5: Fill in the enclosed space in the image. Step 6: Noise reduction steps to reduce artifacts in the image.

CHAPTER 4

EXPERIMENTAL METHODS FOR THE WALKING EXPERIMENT

A walking experiment was designed for the validation of the characteristic settling pattern found in the small-scale paint jet experiment. The experiment measured airflow and chemical signatures at various points along the experimental walking path.

4.1 Experimental setup

A diagram of the setup during the walking experiment is shown in Figure 4.1a with important distances shown in Table 4.1.

Table 4.1: Table to test captions and labels

Element	Distance from start m
1st laser diode	3.38
2nd laser diode	4.68
3.0 m station	6.0
2.0 m station	8.0
1.0 m station	10.0
0.5 m station	12.0
Final cone	20.0

The New Mexico Tech gymnasium was used as the walking experiment's testing area. A curtain was used to split the area into two parts, with one half being the test section and the other being the stand-by area for the walking participants. The length of the walking section was 20.7 m.

Four different sampling stations were set up at distances of 0.5 m, 1 m, 2 m, and 3 m off the walking path on stands made from 20 mm by 20 mm 80/20-compatible t-slotted framing. Anemometers were set at 95 cm from the ground and were held up on converted camera tripods. The walking time through the

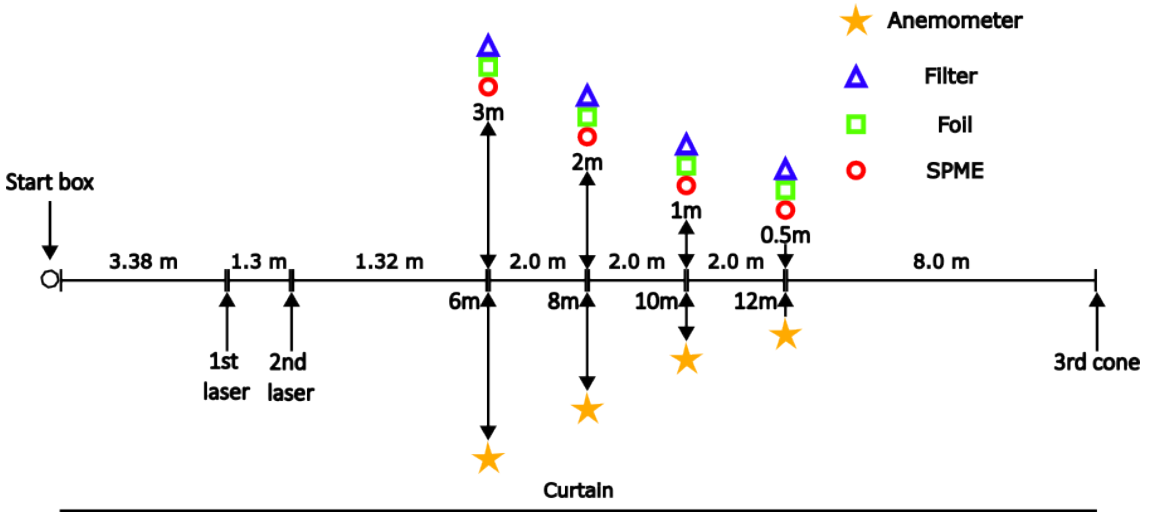

(a)

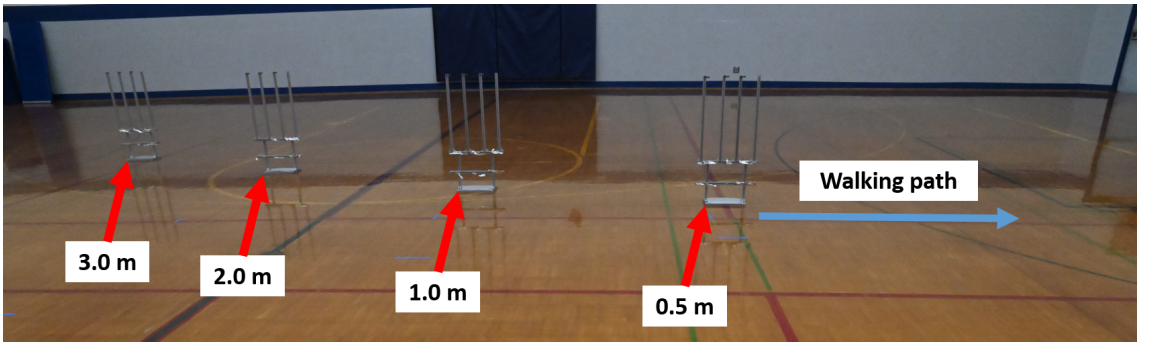

(b)

Figure 4.1: a) Gym diagram from walking experiment. b) Picture of testing stands at the different standoff distances from the first walking experiment.

experimental section was 15 seconds. This was to make each participant's walking speed approximately 1.34 m/s, which was the walking speed used in Edge et al. [6]. A time of 10 seconds was used between each of the walking participants' passes to allow for the wake to settle.

4.2 Walking participants

Participants wore shorts of comfortable length and fitted shirts that exposed their shoulders due to the shoulders being the scaling parameter found by Edge et al [6]. Sunscreen was selected as the contaminant source because its volatile compounds are not commonly found in natural environments. Coppertone Sunscreen Lotion for Kids SPF 70 was applied to the walking participants every 100

passes or before each collection point, whichever came first. To prevent excessive saturation of sunscreen in the experimental environment, participants were required to remain outside the gym for sunscreen application and sample collection unless they were in line for walking passes.

Walking participants were measured to provide sizing used in the analysis. As shown in Figure 4.2, the height, shoulder width, waist height, and waist width measurements were taken. These collected measurements were then averaged and are shown in Table 4.2.

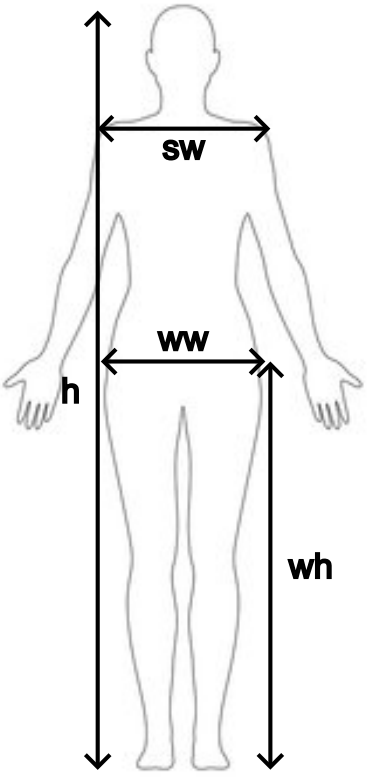

Figure 4.2: Diagram of where measurements were taken on the walking participants, where h is the height, wh is the waist height, sw is the shoulder width, and ww is the waist width.

Table 4.2: Average walking participant dimensions

Height cm	Waist height cm	Shoulder width cm	Waist width cm
176.0	97.8	41.1	33.7

4.3 Testing variations

This experiment was conducted twice: one experiment that spanned one day and another that spanned two days, to address the results from the first experiment. Both experiments had notionally the same test setup, which was outlined in Section 4.1.

The first experiment was conducted to gather knowledge on which chemical analysis techniques were most useful, which test variations were most beneficial, and what could be improved upon in the next iteration. The experiment deployed three SPME arrows at the four standoff locations, as well as a room standard to determine baseline contamination in the gym before the experiment. Set intervals of 200, 500, and 1000 participant walks past each arrow were conducted to increase the introduced signal. In addition, anemometer studies were conducted at the mirrored locations to measure and record the velocity of the trailing wakes behind the walking participants. One SPME arrow, one passive filter, and one witness foil at each sampling station were collected after 200 passes. This process was repeated to create a 500 pass and 1000 pass data set. Table 4.3 shows the data collection scheme.

Table 4.3: Testing scheme for first walking experiment

Walking round	Number of passes	Total number of passes	Collected items
1	200	200	SPME set, filter set, and foil set #1
2	300	500	SPME set, filter set, and foil set #2
3	500	1000	SPME set, filter set, and foil set #3

Table 4.4: Testing scheme for second walking experiment, Day 1

Walking round	Number of passes	Total number of passes	Anemometer dist. [m]	Collected items
1	25	25	0.5	1 SPME @ 1 m
2	50	75	0.5	1 SPME @ 1 m
3	75	150	-	Remaining SPME

Two different walking experiments were performed during the two-day test series. The first day aimed to identify the number of walks needed to reach the saturation point of the SPME arrows and SPME wires used for the data collection. The experiment measured the signal response of 21 SPME arrows and 3

SPME wires at fixed locations and varied the number of participants walking past each arrow to increase the introduced signal. In addition, anemometer studies were conducted at a mirrored 0.5 m location to validate that the anemometer can measure and record the velocity of the trailing wakes behind the walking participants. The main outcome of this experiment was to determine the ideal number of walks required to obtain SPME data without oversaturating the coating and to establish and define the consistency of results across replicate samples. By analyzing the variation in peak area and peak height in SPME measurements from the GC-MS results, the experiment aimed to determine the number of walks needed to produce the best quality data. 1 SPME arrow at the 1 m sampling station was collected after 25 passes, while the remaining deployed SPME arrows and wires were "capped" during a 15-minute break for collection and analysis. The collected SPME arrow was analyzed using a Griffen portable GC-MS. After this analysis, the remaining SPME were "uncapped", and walking participants performed 50 more walking passes before repeating the process of collecting one at the 1 m station, "capping" the remaining SPME, and resting for 15 minutes for analysis. This process was repeated once more with 75 walking passes before the collection of all of the SPME arrows and wires. Table 4.4 shows the data collection scheme.

The second day aimed to measure the spatial and temporal evolution of contamination along a walking path using various collection methods. Contamination was captured using SPME, aluminum foil witness plates, and passive microbial filters to provide a more comprehensive assessment. The same experimental setup of the first experiment was used for both the SPME and anemometer placements. Aluminum foil witness plates were placed at all SPME locations to capture nonvolatile contamination. SPME samples were collected at 75 walking passes, and aluminum foil collection at 500 and 1000 walking passes. The study also included 24 foils, arranged in double triplicate at each sampling station, along with 2 room blanks to measure for background contamination. Anemometer studies were mirrored at each distance. Two studies were done at each distance. Additional studies were done at the 0.5 m and 1.0 m locations due to the data not saving properly on the first replicate. The primary outcome of this test included generating a spatial contamination map using the SPME data, using the first experiment to determine how many walks would be needed to ensure the SPME arrows and wires were not saturated. Additionally, the experiment aimed to compare contamination levels captured by SPME versus foils, assessing whether differences in contamination patterns aligned with expected vapor and particle transport mechanisms. Table 4.4 shows the data collection scheme for the second day of the experiment.

4.4 Sunscreen

To ensure a strong, distinct signal from the sunscreen, a product with a high amount of avobenzenes as one of the active ingredients was selected. The final selection of sunscreen was chosen because of its high amount of octocrylene and

Table 4.5: Testing scheme for second walking experiment, Day 2

Walking round	Number of passes	Total number of passes	Anemometer dist. [m]	Collected items
1	75	75	0.5	SPME
2	125	200	1.0	
3	100	300	2.0	
4	100	400	3.0	
5	100	500	3.0	Foils and filters
6	100	600	2.0	
7	100	700	1.0	
8	100	800	1.0	
9	100	900	0.5	
10	100	1000	0.5	Foils and filters

oxybenzone. This selection ensured that different unique signatures could be traced with the SPME arrows and wires.

The final sunscreen selected was Coppertone Sunscreen Lotion for Kids SPF 70 due to the percentage of key ingredients that could be traced. Table 4.6 shows the percentage of active ingredients in the sunscreen as reported on the manufacturer's container.

Table 4.6: Chemicals present in Coppertone Sunscreen Lotion for Kids SPF 70 and their percentages

Chemical	Coppertone for Kids SPF 70 percentage
Avobezene	3 %
Homosalate	13 %
Octisalate	5 %
Octocrylene	10 %
Oxybenzone	6 %

4.5 Chemical analysis of contaminants

As shown in Figure 4.1a, multiple methods of human contamination detection were used in the Walking Experiment.

One method was using a combination of SPME arrows and wires. This combination of the two types of SPME was due to wanting replication in the experiment, but not having the ability to have a complete set of the same SPME to run

the experiment. The SPME sampling scheme used in the Walking Experiment is shown in Table 4.7. SPME standards were created by warming the Coppertone Sunscreen to 30 °C and then exposing two different dark gray SPME arrows for 10, 30, and 60 seconds. Additionally, standards were created by extracting the Copperton Sunscreen in hexane. The analysis of the SPME was done using a Griffen portable GC-MS.

Passive microbial filters and non-volatile residue (NVR) foils were also deployed as passive collection devices. The passive microbial filters aimed to collect microbes off the walking participants, while the NVR foils aimed to collect any non-volatile residues.

Table 4.7: SPME placement scheme during the walking experiment Day 2

Distance m	Purple arrow	Dark gray arrow	Blue arrow	Silver arrow	Wire	Total arrows	Total wires
3.0	1	1	2	-	-	4	0
2.0	1	1	1	-	2	3	2
1.0	1	1	-	1	1	3	1
0.5	1	1	-	2	-	4	0

4.6 Anemometry measurements

A Kanomax 6501-CE anemometer was used to measure the wake profile that came off each participant as they walked passed each of the sampling stations. Each data collection scheme recorded at least 75 walking passes to ensure that there was a broad distribution of walking participants' wakes that were collected for analysis. The anemometer sampled in analog mode, outputting a voltage value between 0 and 1. The anemometer has an analog sampling rate of 0.1 s or 10 Hz. A NI-9201 voltage card from National Instruments was used to read the voltage output of the anemometer during each pass. This was interfaced with National Instruments FlexLogger software to record the values at a frequency of 0.005 s or 200 Hz to ensure that the voltage output was recorded. This was done to ensure that the software was able to record the output value since the frequencies were not in sync with each other. Known conversion factors given in the anemometer user manual were used to convert the recorded voltages to convert them to air velocities. Each walking round was 100 walking passes before resetting, except for the first two rounds. Table 4.5 shows when the anemometer was deployed and at what distance.

CHAPTER 5

RESULTS FOR PAINT JET EXPERIMENT

5.1 Jet image processing

Image processing used to quantify the concentration of paint onto the bottom of the test section, using the identified area of interest, was done on an image after 235 seconds of continuous spray for z_0, which Figure 5.1 shows a 3D representation of these paint concentrations. Final depositions for all three heights are shown in Figure 5.2, which depicts how the depositions vary as the height changes.

The paint concentration graphs were normalized by the local peak concentration, which is shown in Figure 5.3c. As shown by Hussien et al [39], the mean streamwise velocity for an axisymmetric jet is self-similar. The local maximum velocity of the jet is the maximum, and the velocity decays symmetrically on both sides to zero. And since velocity and mass transfer are related through RTT, this relationship can be used for the jet spray deposition data sets. A nondimensional location parameter, which is denoted with η, was defined as the ratio between the spanwise coordinate, denoted with r, and the adjusted streamwise coordinate, denoted with s, which is shown in Equation 5.1. The spanwise coordinate is adjusted with a parameter called the "virtual origin", which is denoted with s_0. Figure 5.3b shows where the different parameters are in relation to the spray jet.

$$\eta = \frac{r}{s - s_0} \tag{5.1}$$

Table 5.1: Analysis of the different airbrush configurations

	Region	Nozzle height, z cm	Virtual origin mm	Spreading half angle deg
z_0	1	12.07	13.00	12.0
z_0	2	12.07	37.65	17.5
z_1	-	21.87	55.56	22.0
z_2	-	28.35	64.79	30.0

Edge detection was done through a combination of background subtraction, thresholding, and morphological processing. First, the background image was

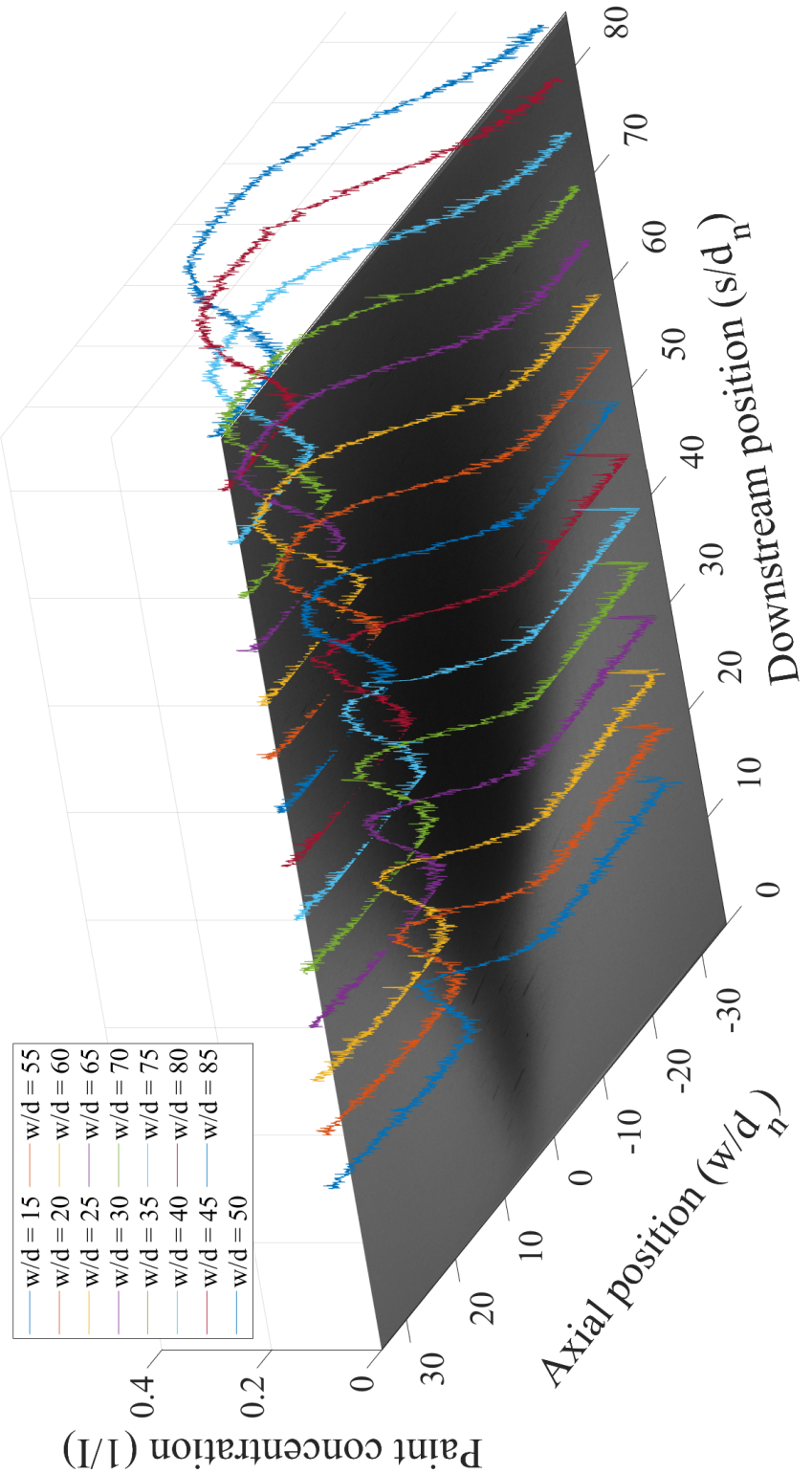

Figure 5.1: 3D graph of the area of interest concentrations versus normalized axial position versus normalized downstream position, where w is the width of the test section and l is the length of the test section. 1/I is the paint concentration on the z-axis.

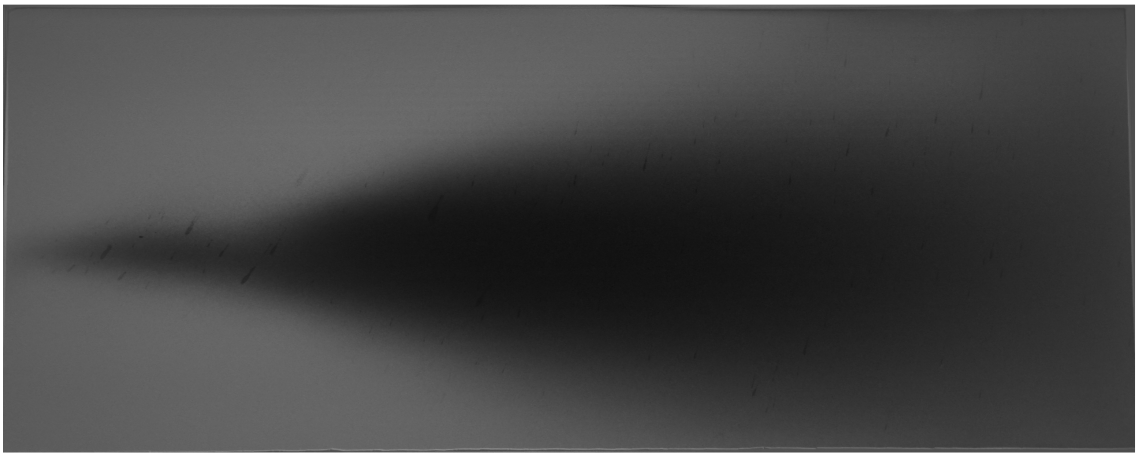

(a)

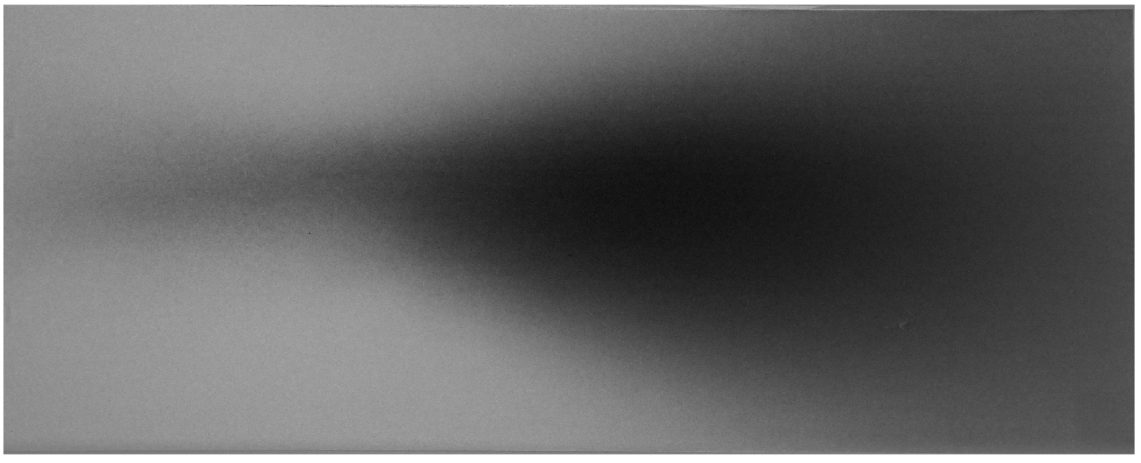

(b)

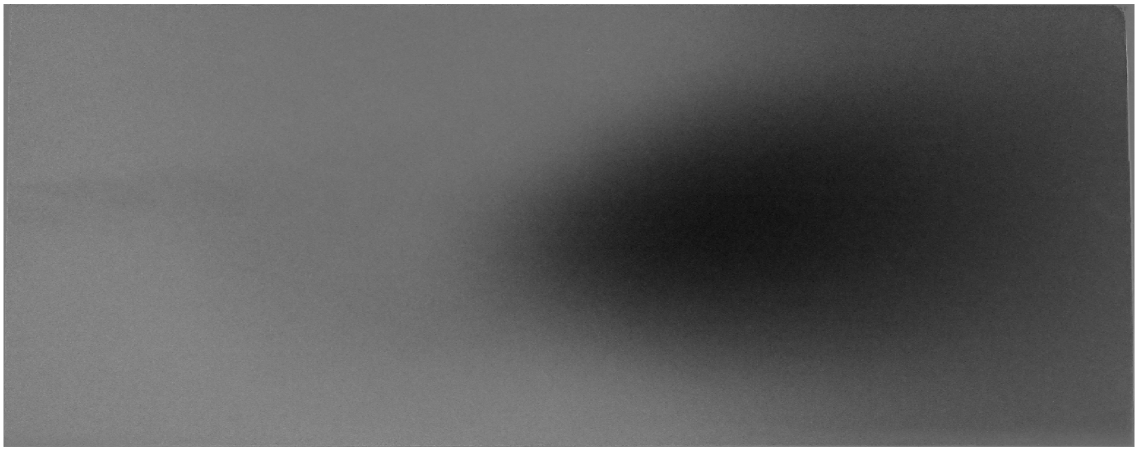

(c)

Figure 5.2: a) Paint deposition for z_0. b) Paint deposition for z_1. c) Paint deposition for z_2.

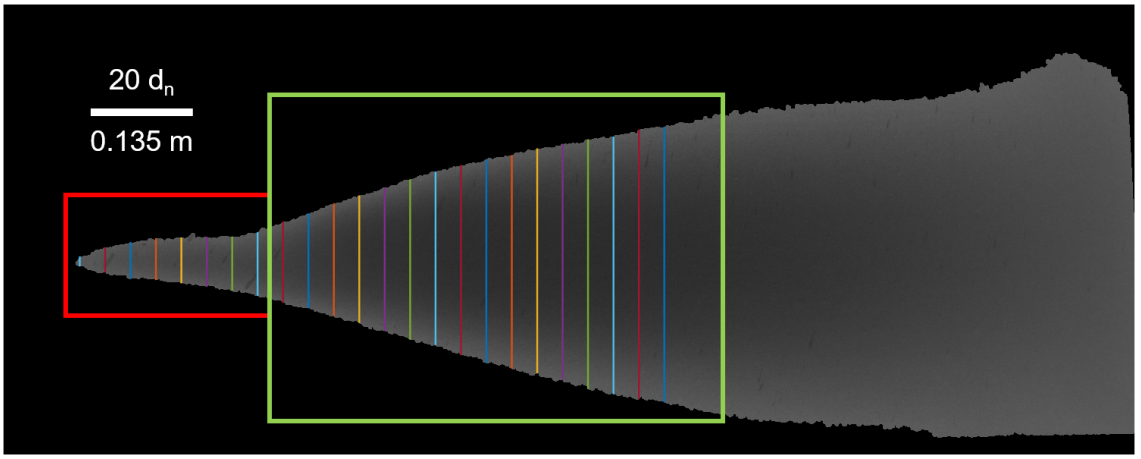

(a)

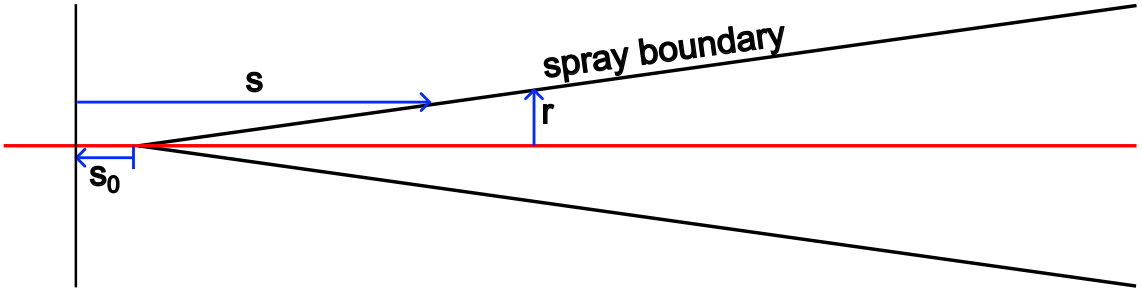

(b)

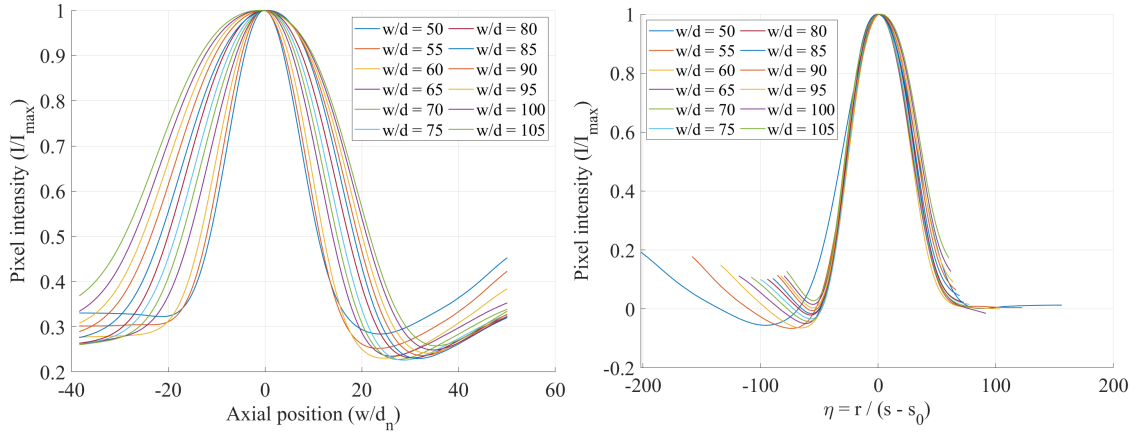

(c) (d)

Figure 5.3: a) Paint deposition for z_0 with analysis lines drawn at 5 diameter spacing from w/d = 10 to w/d = 125. b) Diagram of paint spray and where the jet scaling parameters are relative to the spray boundaries. c) Pixel intensity versus axial intensity for z_0. d) Pixel intensity versus similarity coordinate η, collapsed using s_0= 37.65 mm for z_0 in region 2.

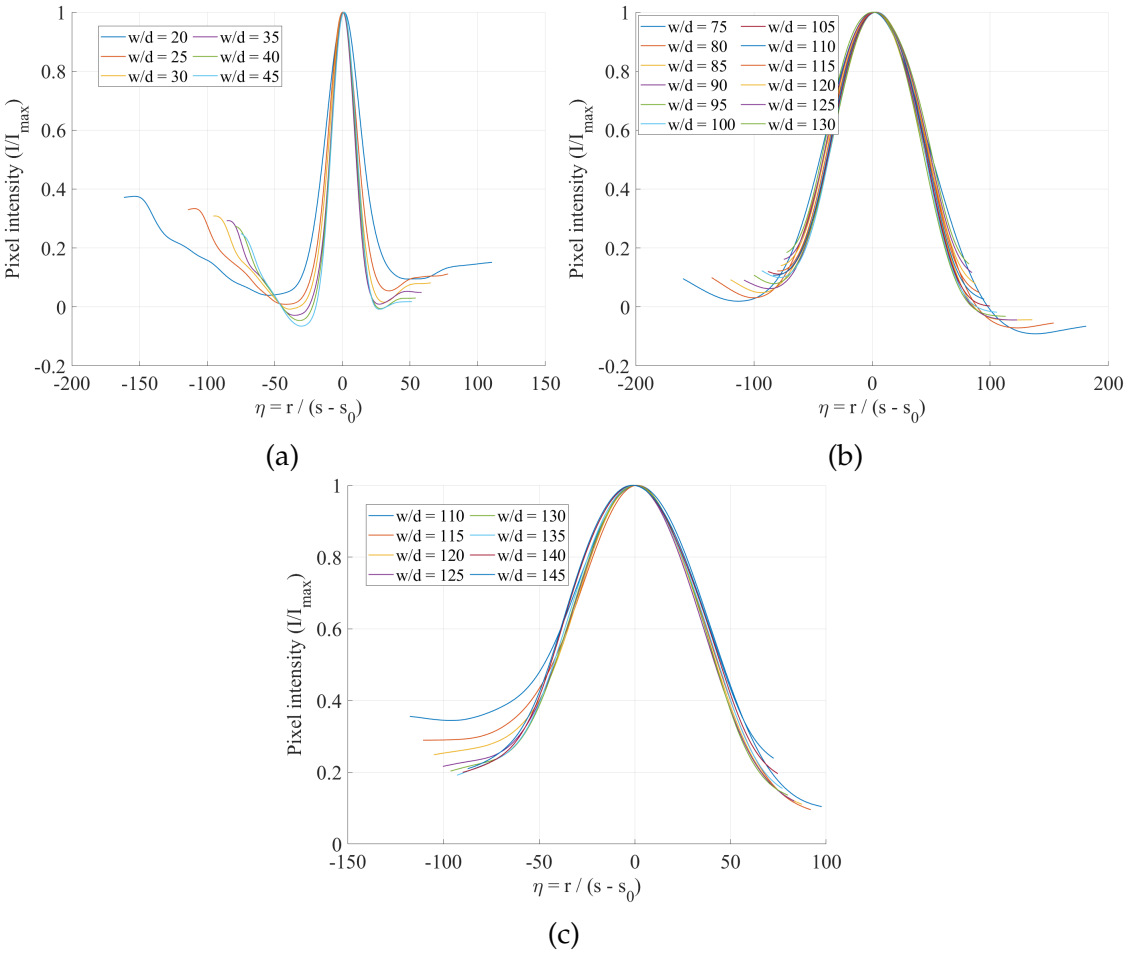

Figure 5.4: a) Pixel intensity versus similarity coordinate η, collapsed using s_0= 13.50 mm for z_0 in region 1. b) Pixel intensity versus similarity coordinate η, collapsed using s_0= 55.56 mm for z_1. c) Pixel intensity versus similarity coordinate η, collapsed using s_0= 64.79 mm for z_2.

subtracted from the data image to reduce background noise. The resulting difference image was then binarized using a global threshold to create a mask of regions of interest, which was refined by filling holes and applying morphological opening to remove small noise. This binary mask highlights significant regions, which were then used to filter the original difference image, isolating only relevant features.

Looking at 5.3a, which outlines the edge of the spray deposition for z_0, two different regions of the spray deposition can be seen. The first region is from 20 to 45 nozzle diameters downstream, and the second region is 50 nozzle diameters downstream to the end of the spray deposition. However, due to the edge of the spray test box impacting the spray deposition, the farthest downstream position that was analyzed was 105 diameters downstream. To characterize these

two regions, the virtual origin and the spreading half-angle for each region were found. The virtual origin was determined by an iterative process of substituting varying multiples of the nozzle diameter into Equation 5.1 and determining if the resulting curves stack on top of each other to form a single profile using an optimization routine, and Figure 5.3b shows this relationship. Investigation into this led to the two different regions having different virtual origins, reinforcing the notion that there are two separate regions in this deposition.

With this process, the graph of the intensities shown in Figure 5.3c for z_0 turns into Figure 5.3d with a virtual origin of 5.58 nozzle diameters or 37.65 mm with a nozzle diameter of 6.75 mm for the second region. This was also done for region 1 and the other two experimental heights, z_1 and z_2, which are shown in Figure 5.4. The spreading half-angle was found by finding the edge of the spray deposition and using MATLAB to measure the angle. Due to the assumption that the jet is axisymmetric, this measurement is divided by two to find the half angle. Table 5.1 shows a comparison of the virtual origin and spreading half angles found for the 4 different cases. Comparing the difference between the height and the virtual origins that were found for z_1 and z_2, the virtual origin for the second region of z_0 follows the trend more than the first region. Because of this, region 2 will be used for the remainder of the analysis.

Additional analysis was done on the spray deposition images to include downstream analysis. The same process that was used to analyze the radial paint depositions from the jet was used for the downstream analysis. In this analysis, the row of pixels was pulled parallel to the centerline of the spray deposition. The reference location for the downstream analysis was the centerline of the paint spray field instead of the nozzle location. This analysis highlights the ramp-up of paint deposition and where the concentration levels out. These trends are shown in Figure 5.5.

Downstream analysis was done for all 3 heights to compare the depositions to each other, which is shown in Figure 5.6. This shows that the peaks do not align, which is expected since the virtual origins differ. The z_0 plot reaches its maximum first, then the z_1 plot, and finally the z_2 plot. Since the axial depositions were able to be scaled with the virtual origin, the scaling for the downstream position should also be the same and used for all three cases.

The Buckingham Pi analysis found a length over a characteristic length. This Π was leveraged to scale between the three different heights. Since each deposition has a unique virtual origin, the length of each deposition was nondimensionalized with this value. This nondimensionalization aligned the leading slopes and peaks of each deposition.

Scaling for pixel intensity was explored next. Since this analysis flipped each image matrix so that the light regions were associated with low values and dark regions were associated with high values. These dark regions were also associated with paint deposition, which could be measured with a mass per area. Because of this, it was assumed that pixel intensity is proportional to a given mass per area, which is shown in Equation 5.2. Since the depositions are characterized by the number of nozzle diameters from the same exit nozzle location, the nozzle

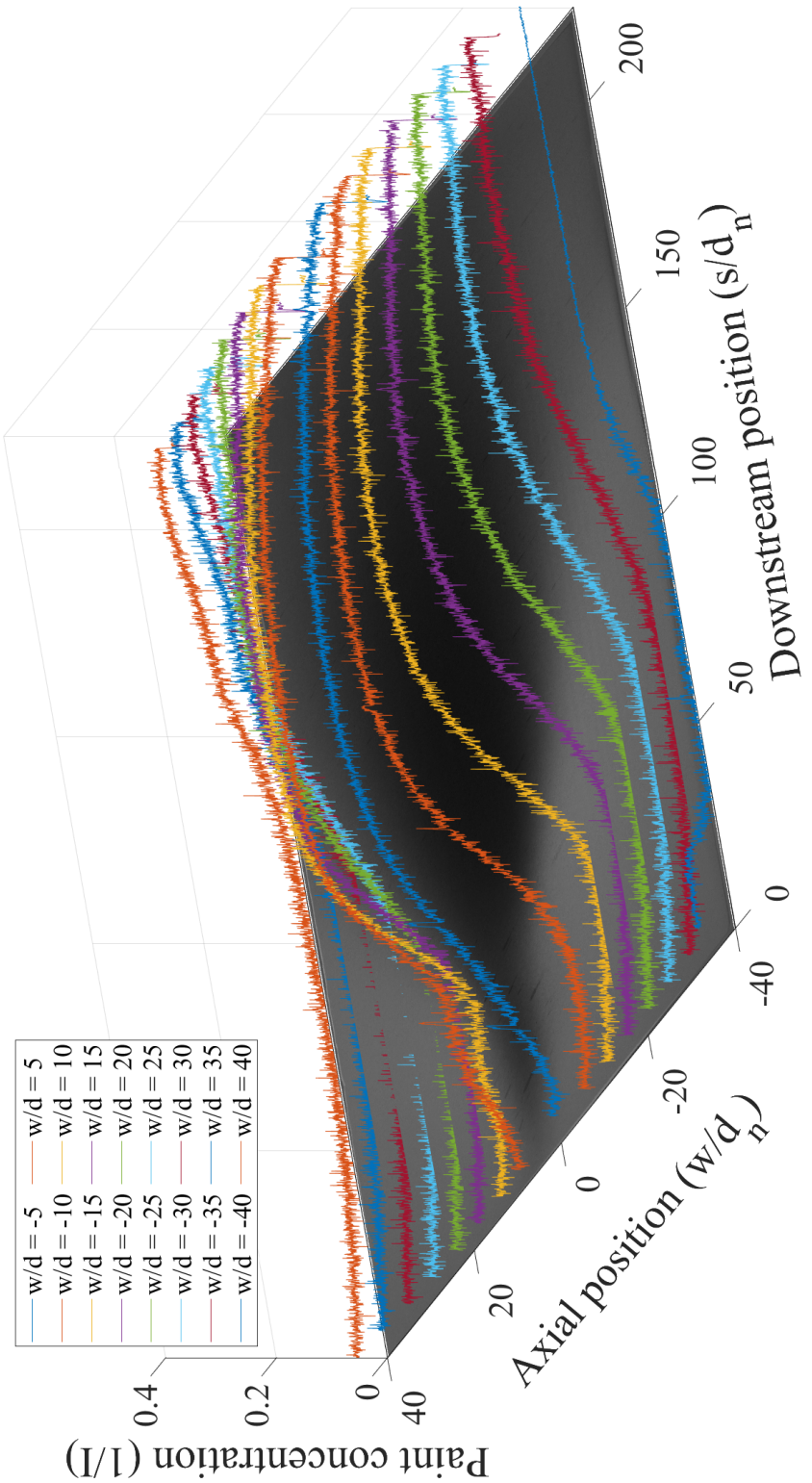

Figure 5.5: 3D graph of downstream deposition profiles versus normalized axial position versus normalized downstream position, where w is the width of the test section and s is the downstream position. 1/I is the paint concentration on the z-axis.

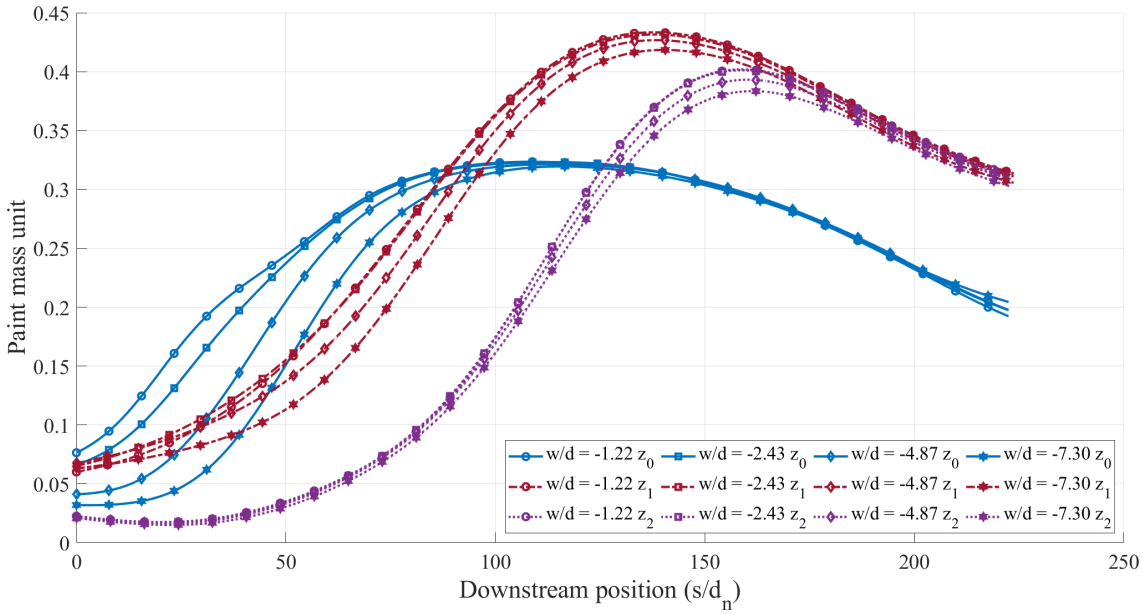

Figure 5.6: Graph comparing the spray depositions of the three different height cases.

diameter was used as the characteristic length to calculate the square area of a location in the deposition field.

$$I = pixel\ intensity \propto \frac{m}{A} \tag{5.2}$$

The intensity can be turned into a mass unit by multiplying the pixel intensity by the nozzle diameter squared, with this relationship. The y-axis was normalized by dividing the mass values by the peak mass value, just like what was done in the axial jet scaling. The end relationship is shown in Figure 5.7.

5.2 Paint droplet characterization

Analysis to determine the trends and statistics of paint that was deposited onto the glass slides was done using visual inspection and image processing. Visual inspection was done to note qualitative trends, and image processing was done to note the quantitative trends within the deposition.

For visual inspection, one image per testing location was examined. In the Burst test case, droplets $\geq$2 μm in diameter did not appear until 35 nozzle diameters downstream on the centerline and 25 in one axial direction. Droplets were not consistently seen across the field until 85–95 nozzle diameters downstream. These observations are shown in Figure 5.8.

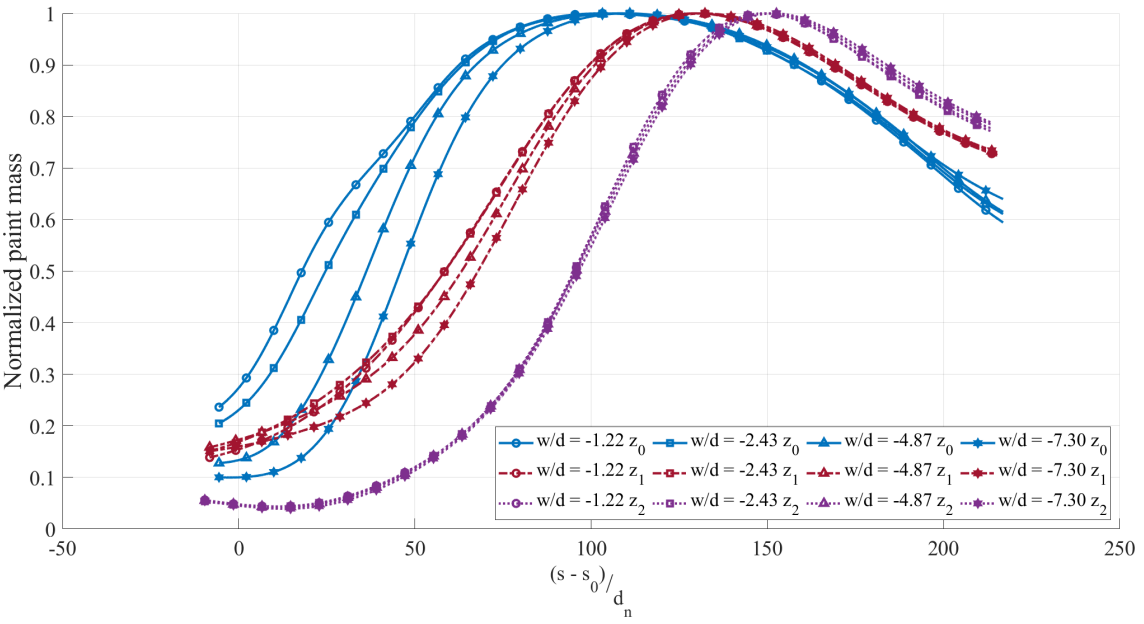

Figure 5.7: Graph comparing the spray depositions of the three different height cases where the downstream position, s, is scaled by the virtual origin, s_0.

In the 1 second case, droplets $\geq$2 μm appeared at 25 nozzle diameters downstream along both the centerline and one axial direction. Broader spray coverage was observed at 65 nozzle diameters. Deposition density increased along both centerline and radial directions, with a downward trend in droplet size beyond 35 nozzle diameters and radially outward. Figure 5.9 displays the observations.

In the 3 second case, droplets $\geq$2 μm were seen at 15 nozzle diameters on the centerline and 25 in one axial direction. Spray field coverage became consistent at 65 nozzle diameters. Deposition density increased along both directions, with droplet size decreasing beyond 35 nozzle diameters and radially. See Figure 5.10.

In the 5 second case, droplets $\geq$2 μm were present at 25 nozzle diameters along both the centerline and one axial direction. Full field coverage appeared at 75 nozzle diameters. Deposition density increased throughout the spray field, with droplet size decreasing downstream and radially. Observations are shown in Figure 5.11.

Based on the microscope images, a large amount of paint deposition did not appear to reach the glass slides until approximately 35 nozzle diameters downstream for all four test cases. This is in line with the results from jet image processing, where near-field regions of 0 to 45 diameters are ignored due to being in region 1 of the spray deposition, which has a virtual origin that does not follow the same trends found in the two other height variations. Paint particle size decreases downstream as well as radially, which is in line with Stokes number.

Image processing determined the paint particle diameter for the four test cases at the forty-seven testing locations: nine centerline locations and 19 mir-

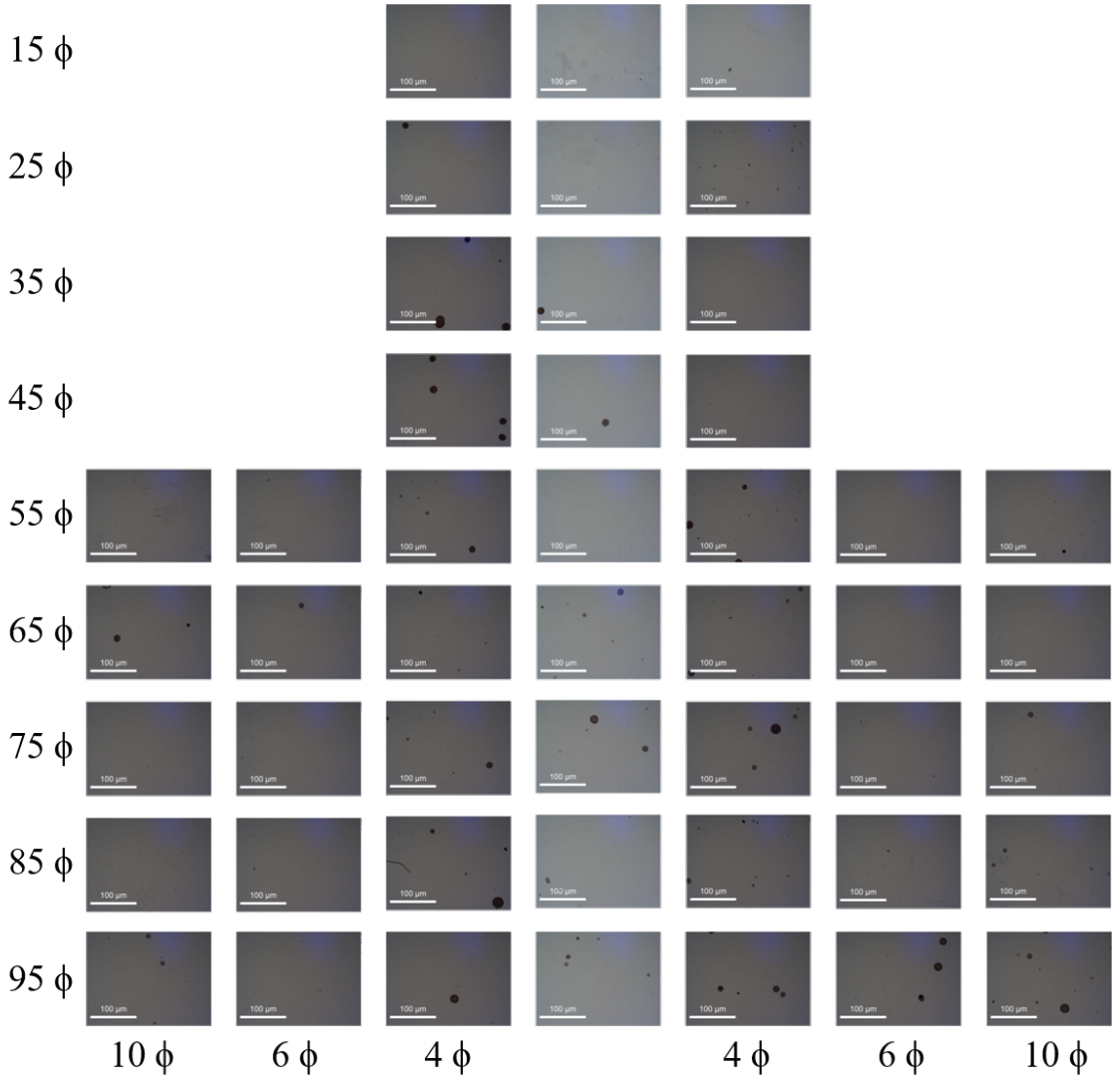

Figure 5.8: Tiled image of some of the microscope pictures from the burst test.

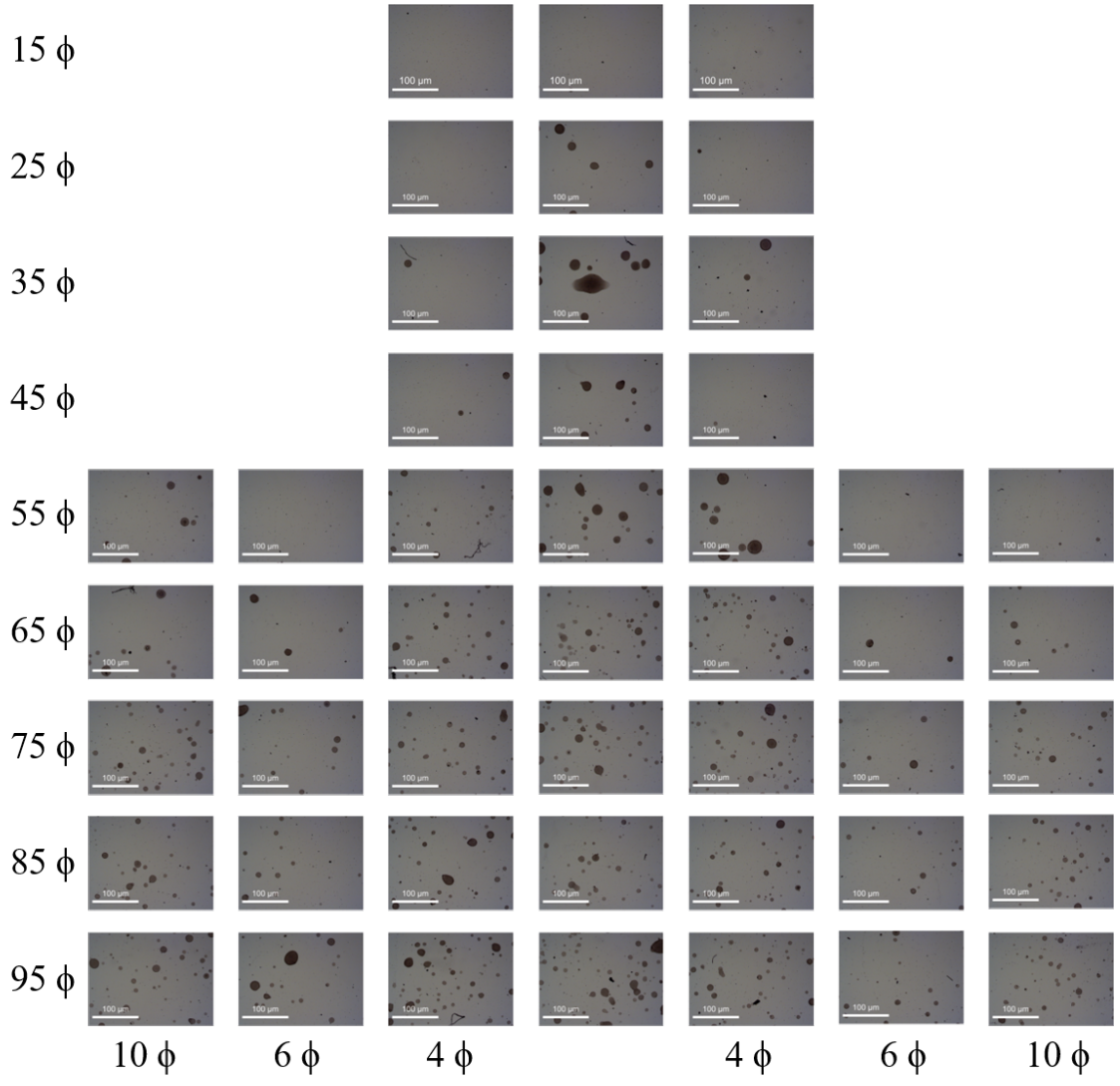

Figure 5.9: Tiled image of some of the microscope pictures from the 1-second test.

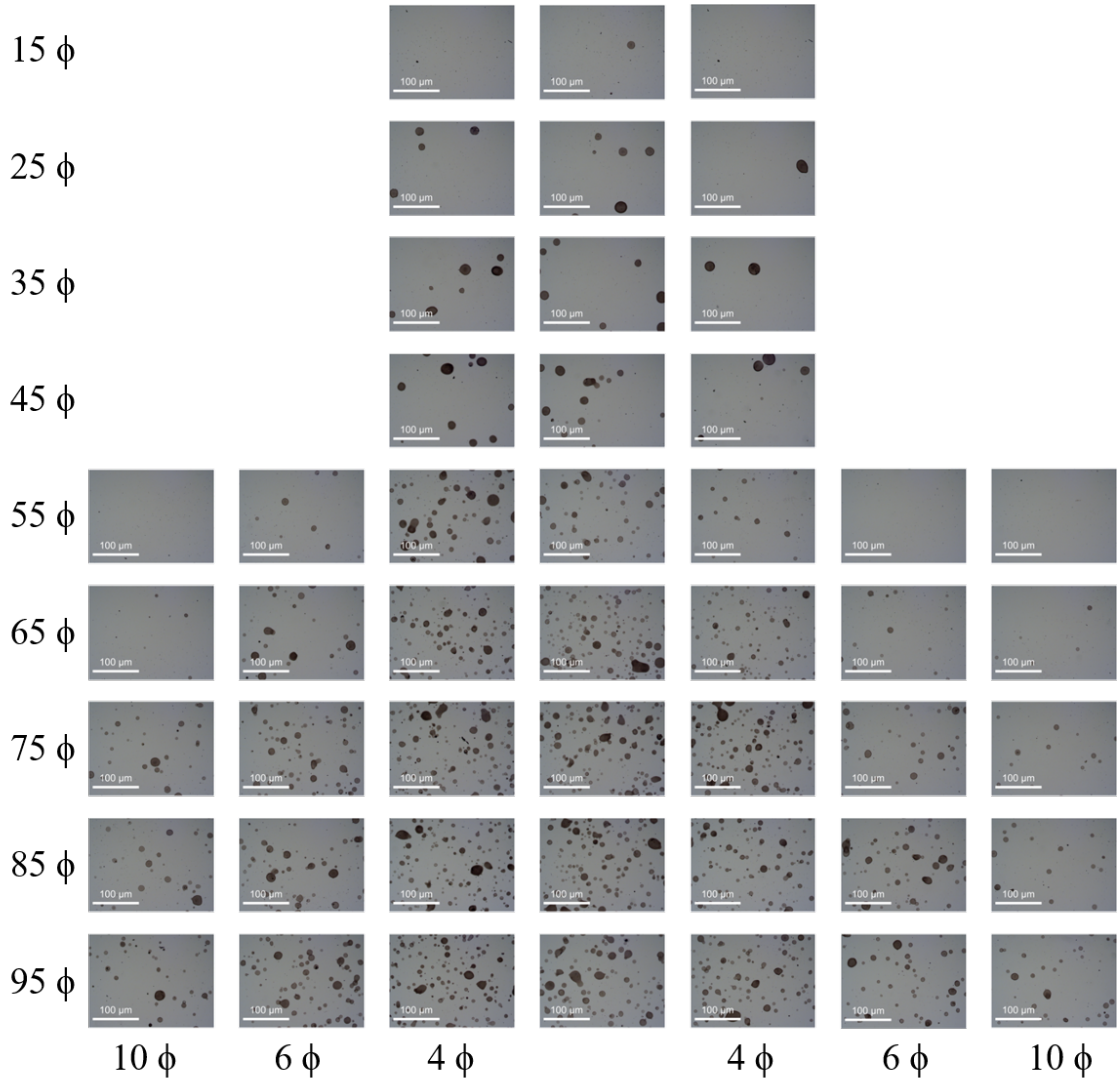

Figure 5.10: Tiled image of some of the microscope pictures from the 3-second test.

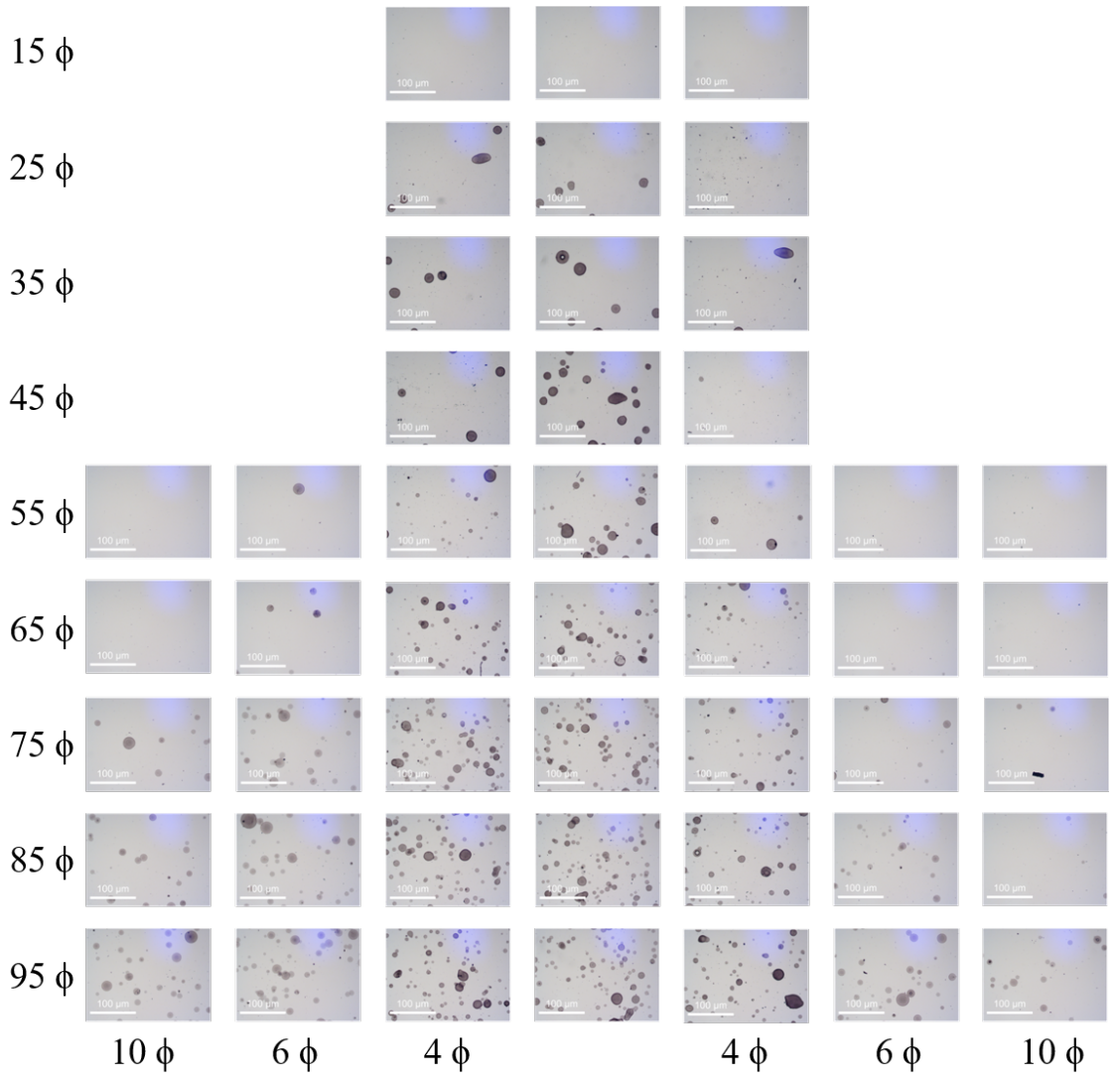

Figure 5.11: Tiled image of some of the microscope pictures from the 5-second test.

rored axial locations. The nine centerline locations were 15 to 95 nozzle diameters spaced 10 nozzle diameters apart. The axial positions were defined with the centerline set to 0, and radial distances extending symmetrically outward at 4, 6, and 10 nozzle diameters from the centerline in both directions. It is important to note that all images analyzed for paint particle sizing measured the dry paint particle size on the surface of a glass microscope slide.

To get statistics from each location, an image was only used if there were 25 paint droplets or more in the image. Due to this thresholding, images from the near-field diameters of 15 to 35 nozzle diameters were not analyzed, and some cases did not have analysis until 55 nozzle diameters downstream. This is due to there not being enough large paint droplets, and the small paint artifacts that were deposited being filtered out with image processing as noise. Additionally, the 6 nozzle diameters from centerline positions at 45 nozzle diameters and the 10 nozzle diameters from centerline at the 55 nozzle diameters radial positions were not analyzed for the same reason. The Burst test case data was not analyzed due to the thresholding. Figure 5.12 shows the average size at each downstream position as well as the calculated standard deviation. Because a jet is assumed to be axisymmetric, the data were analyzed and plotted for the absolute value of the radial position. Figure 5.13 shows the average size at the different radial positions as well as the calculated standard deviation. It is important to note that the standard deviation decreases in the downstream positions, indicating a more uniform sizing among the particles.

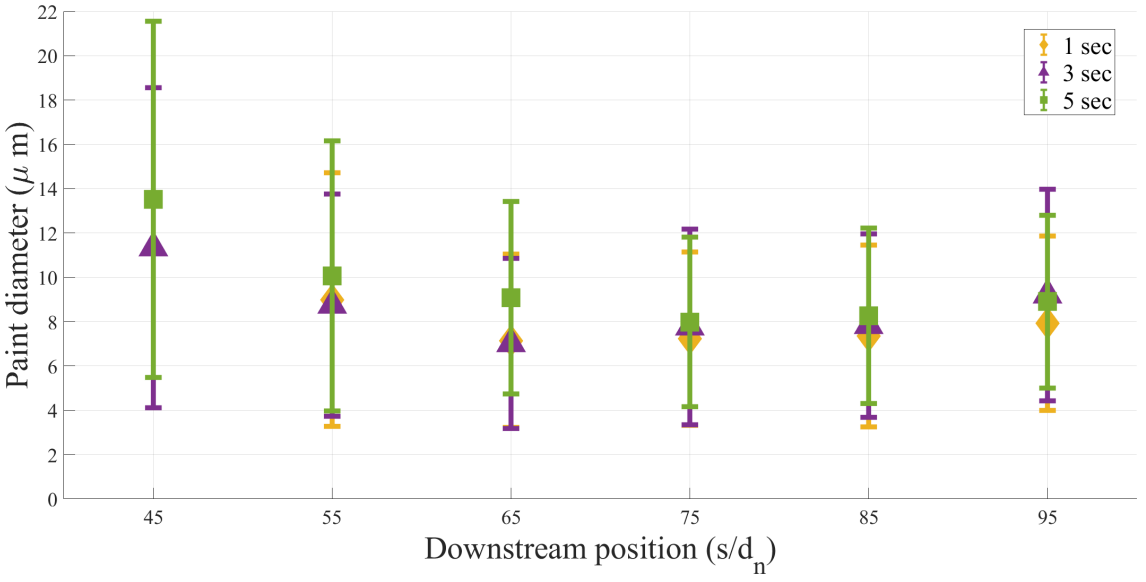

Figure 5.12: Average paint diameter versus downstream position from the exit nozzle normalized with the nozzle diameter for the 1 second, 3 second, and 5 second test cases

The paint droplet diameters found from the microscope images were then used to calculate the corresponding Stokes number, which is shown in Figure

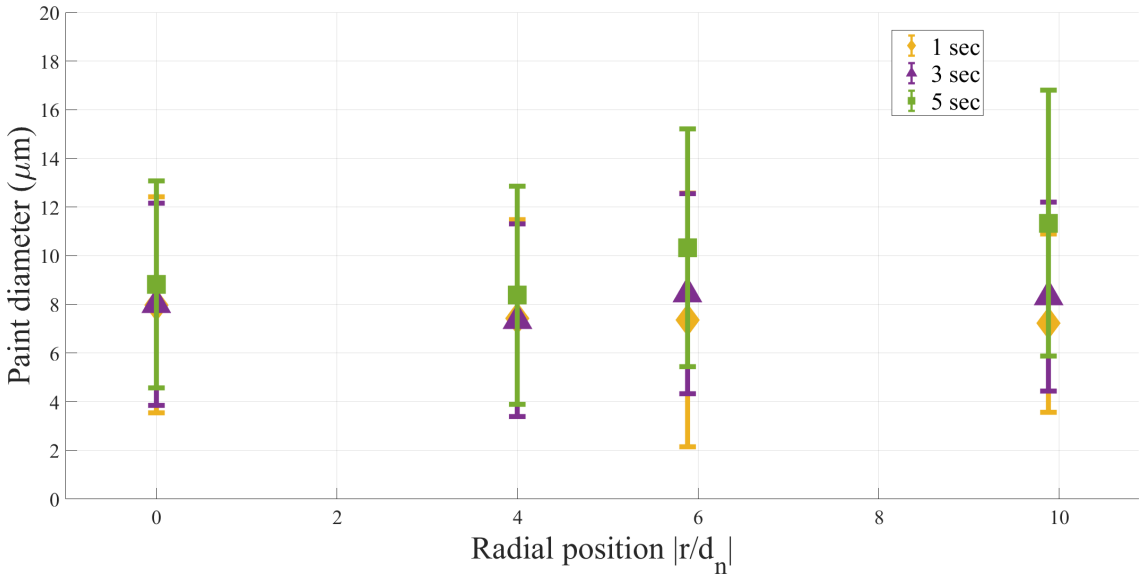

Figure 5.13: Average paint diameter versus axial position from the center of the exit nozzle normalized with the nozzle diameter for the 1 second, 3 second, and 5 second test cases for the downstream positions of 55 to 95 nozzle diameters.

5.14. These calculated Stokes numbers were then related to pixel intensity to create a map across the image. In order to do this, the non-inverted pixel intensity was plotted against the centerline row of Stokes number to see if there was a trend, which is shown in Figure 5.15. In this plot, it appears that both the downstream pixel intensity and the downstream Stokes numbers have the same general shape. This means that downstream, as the pixel intensity gets darker, the Stokes number gets smaller, which is expected as smaller particles will stay suspended in the paint jet longer than larger particles. Standard error was calculated for Stokes number, shown with the error bars in Figure 5.15. Standard error, shown in Equation 5.3, is a method of quantifying the variability across multiple statistical data sets. This method provides insight into how much an estimated value is expected to deviate from the population. Another way to interpret this type of error is that it measures the mean precision across multiple samples.

$$SE = \frac{\sigma}{\sqrt{n}}, n = number\ of\ occurances \tag{5.3}$$

With this in mind, a relationship for Stokes number derived from intensity was created. To isolate a mass per area, which was assumed to be proportional to the intensity, the density of the particle was pulled out front to be the mass of the particle over the volume of the particle. This relationship is as follows:

$$Stk = \frac{\rho_p d_p^2 u_f}{18 \mu_f d_n}$$

$$\rho_p = \frac{m_p}{V_p}$$

$$1 = \frac{A_n}{A_n}$$

$$Stk = \frac{m_p}{V_p} \cdot \frac{d_p^2 u_f}{18 \mu_f d_n} \cdot \frac{A_n}{A_n}$$

$$Stk = \frac{m_p}{A_n} \cdot \frac{d_p^2 u_f}{18 \mu_f d_n} \cdot \frac{A_n}{V_p}$$

Key assumptions are shown below:

- Intensity is proportional to a mass per area
- Area is the nozzle diameter squared
- Volume is the volume of a sphere with a diameter of d_p

The final relationship is shown as follows:

$$Stk = I \frac{1}{d_p} \frac{u_f d_n}{3\pi\mu_f} \tag{5.4}$$

To validate this, the relationship was plotted. However, the calculated Stokes numbers, while following the same trend as seen in Figure 5.14, were significantly smaller. However, by normalizing the pixel intensity, the same trend was found. The results of Equation 5.4 with the applied pixel intensity normalization are shown in Figure 5.16.

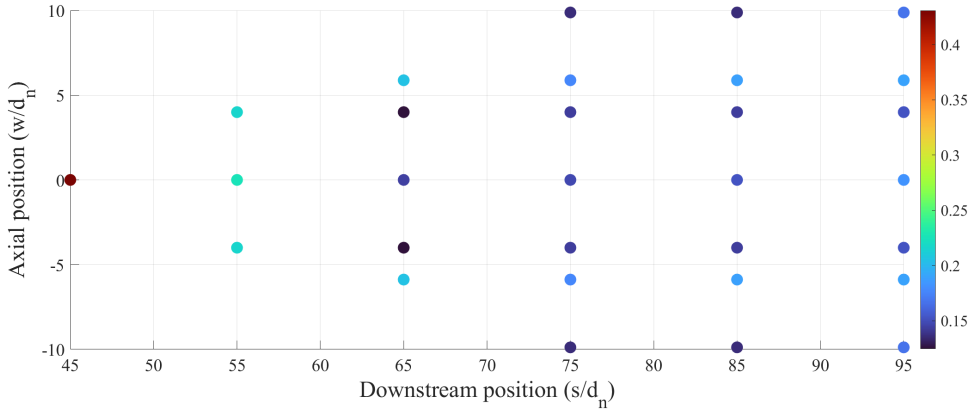

Figure 5.14: Stokes map of the paint particle deposition onto the microscope slides.

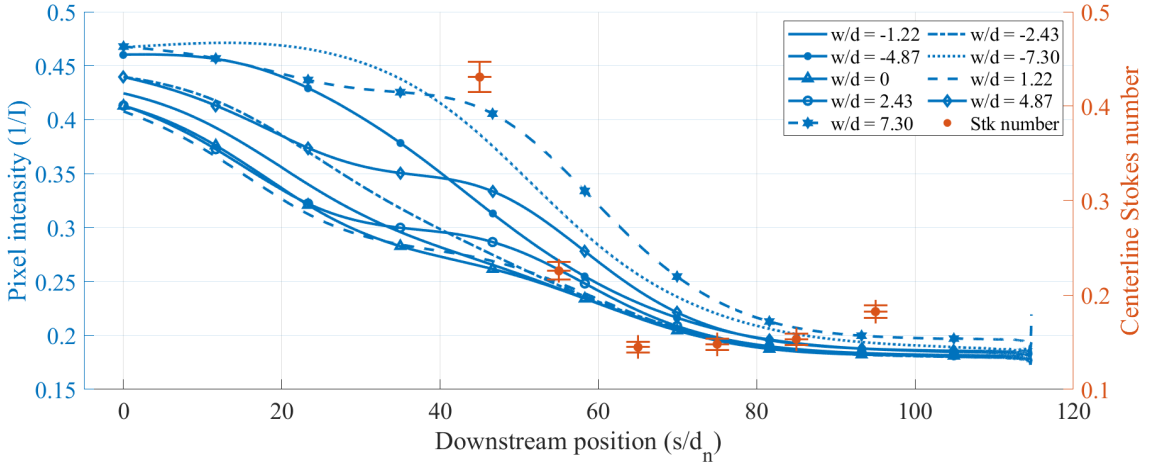

Figure 5.15: Plot of pixel intensity for z_0 and found Stokes number versus downstream position normalized with exit nozzle diameter.

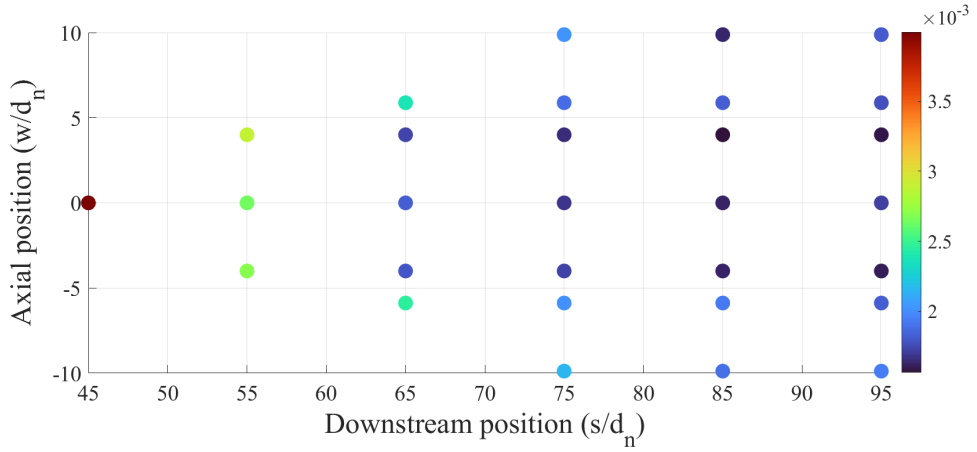

Figure 5.16: Calculated Stokes map of the paint particle deposition using the paint diameters from the microscope slides

CHAPTER 6

RESULTS AND DISCUSSION FOR WALKING EXPERIMENT

6.1 Walking participants

Average walking speed measurements were taken in two different ways. One was with a timing gate for sports training applications, and the other was with two laser diodes. The sports timing gate printed out the time it took for each walking participant to walk from the first cone to the last cone. The laser diode method gave the time it took the participants to walk from the second cone to the third cone. This gave the average walking speed right before the participant entered the test section and passed by the 3 m sampling station. The laser diode also provided a timestamp for when the walking participant entered the testing section, which was useful for pulling the HAW profiles in the anemometer recordings. The times recorded were then converted to walking speed by dividing the distance traveled by the times recorded. While the participants were instructed to walk at approximately 1.34 m/s, the actual average walking speed for a walking pass was 1.58 m/s from the timing gate method and 1.44 m/s from the laser diode method before entering the test section. Figure 6.1 shows the distributions in walking speed throughout the experiment. The histograms used the calculated standard deviation of each data set for the bin width.

While the laser diode method provided a more accurate measurement, the sports timing gate found the time it took to traverse the entirety of the experimental setup from the first cone to the last cone. In contrast, the laser diode method only recorded a short section of time before entering the experimental section. Because of this, the walking speed found from the sports timing gate method will be used for the remainder of the calculations.

6.2 Chemical analysis of contaminants

It is important to note that the SPME arrows used in the first diagnostic experiment were analyzed with a different GC-MS than the SPME arrows used in the second, two-day experiment. This was due to wanting more rapid analysis of the SPME arrows, which is why the Griffen portable GC-MS was used.

To demonstrate that the SPMEs were not saturated after deployment during the experiment, a headspace experiment was done by exposing an SPME arrow to

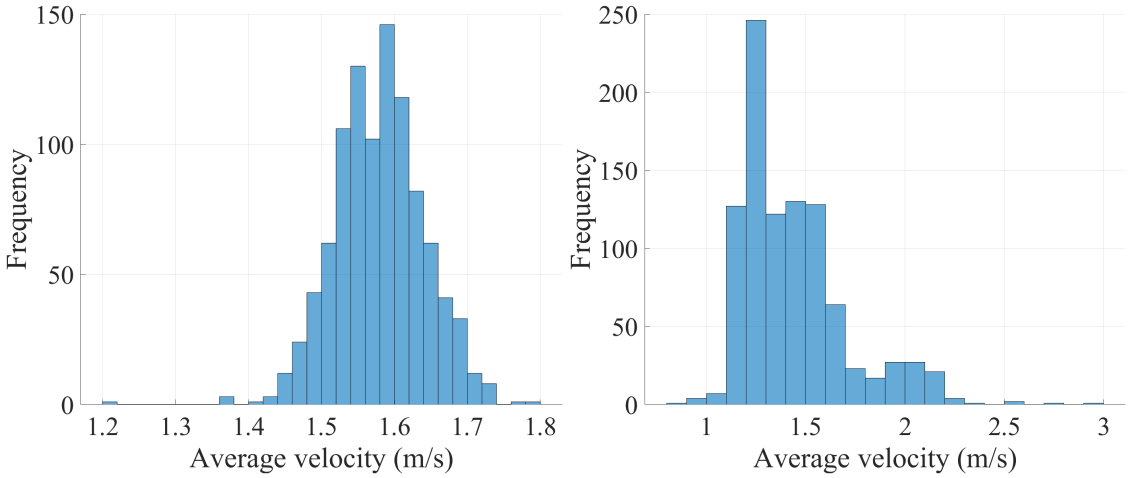

Figure 6.1: a) Participant walking velocity distribution for speed tracking for the full walking pass with a mean value of 1.58 m/s, $\sigma = 0.06$. b) Participant walking velocity distribution for speed tracking before entering the test section with a mean value of 1.44 m/s, $\sigma = 0.27$.

a vial containing sunscreen covered with a diaphragm at different time intervals of either 10, 30, or 60 seconds. Various peaks in these created sunscreen peaks were identified at different retention times (RT). The longer an SPME arrow was exposed to the sunscreen, the higher these key peaks were. Figure 6.2 shows these trends in the standard as well as the target analytes.

All of the SPME arrows and fibers were analyzed. However, due to instrumentation issues, not all of the data files were recoverable from the Griffen. Therefore, not all of the data could be used to identify trends.

More specifically, this was used to show that the SPMEs were not saturated and that the accumulated material increased with time. The peak areas from the walking experiments were far smaller than even the 10-second exposure

The SPME arrows that were deployed for 125 walks on Day 1 were the arrows analyzed in addition to the SPME arrows that were deployed for 75 walks on Day 2. The 125 pass experiment on Day 1 of the walking experiment produced larger peak areas than the 75 pass experiment, which were both significantly smaller, as shown in Figure 6.5. Siloxanes were also detected in the collected samples, but not in the sunscreen standards. Siloxanes are common contaminants found in lubricants and personal care products, meaning these could have been introduced by the walking participants or from the experimental stands. The gym environment may have also introduced these volatiles as background contamination that was not detected in the gym standards. From this analysis, three different peaks were identified based on their RT positions in comparison to the sunscreen standard. The presence of the three sunscreen peaks was seen in the analysis for all distances for both the 125 walk SPME arrows and the 75 walk

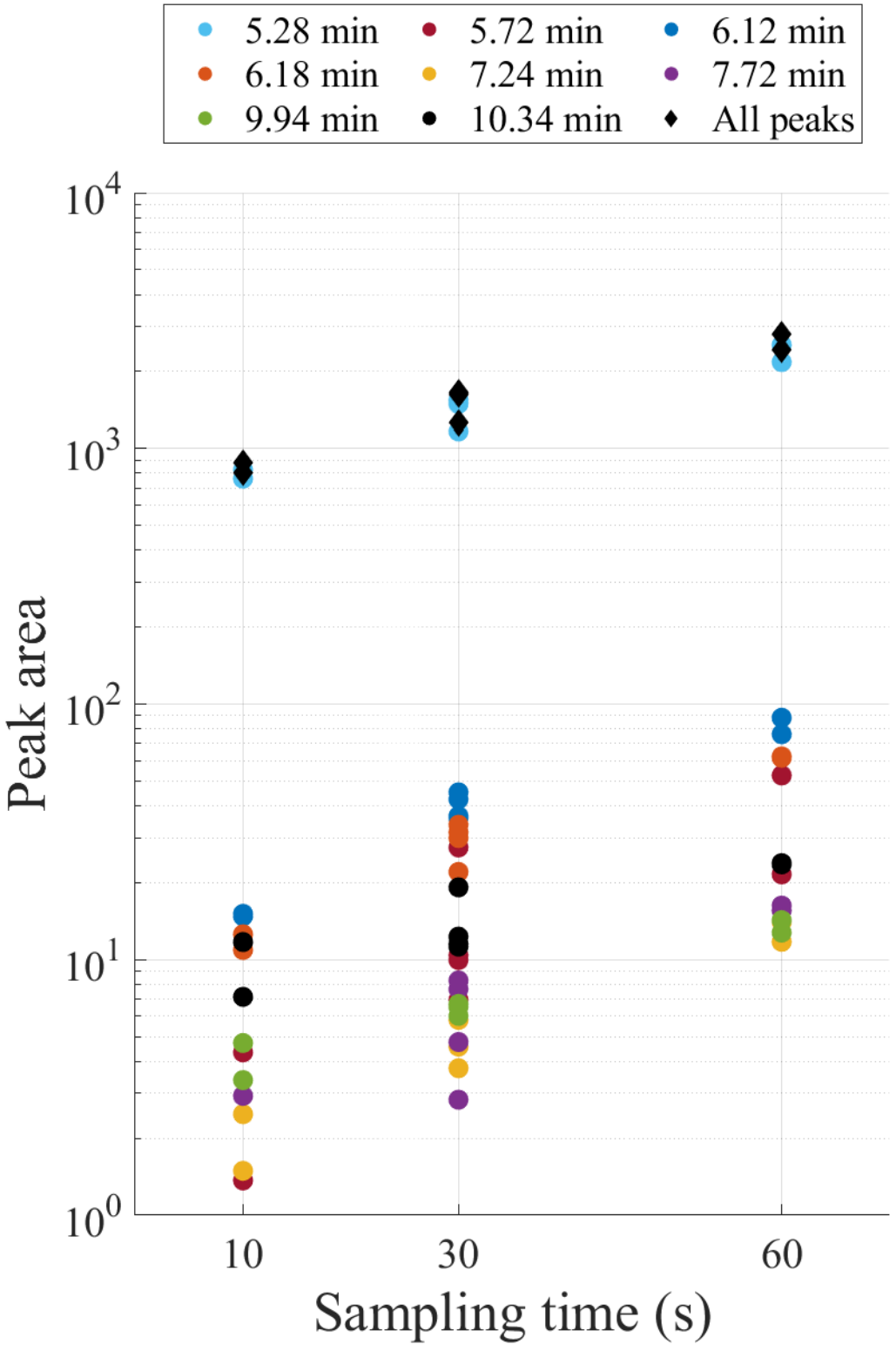

Figure 6.2: Peak area vs sampling time for sunscreen headspace measurement. Time in the legend represents the retention time of that peak.

SPME arrows. These results indicate that the volatiles were dispersed throughout the experimental setup. These peaks were normalized to calculate relative abundance with two different methods: one method normalized with siloxane, shown in Figure 6.3, and one normalized with the total peak area of the identified peaks, shown in Figure 6.4.

The SPME data show no indication of saturation at any of the locations from Day 2 of the walking experiment because the peak areas calculated for the experimental samples were smaller than those calculated in the sunscreen standards. Looking at both methods for calculating relative abundance, a nominal downward trend can be seen in the data as sampling distance increases. It is important to note that after 75 walking passes, there was a substantial amount of analyte at each distance. This trend is shown in Figure 6.5. Further investigation into the background contamination present in the gym is needed to determine the source of background contamination that may have influenced the relative abundance calculations.

6.3 Other chemical analyses

In contrast to the SPME arrows, the NVR foils only showed sunscreen presence after 1000 walking passes, with roughly equal abundance at 0.5 m, 1 m, and 2 m sampling locations, and a significant decrease at the 3 m sampling location. In addition, residue was observed at the 1 m sampling location after 500 walking passes, while no sunscreen residue was detected at any testing location on the 200 walking pass foils. However, it is important to note that the 500 walking pass data cannot be directly compared to the 1000 pass walking data due to the sets being analyzed on different instruments.

The passive microbial filters revealed extractable microbial DNA, presumed bacterial cells from the walking participants, only after 1000 walking passes and only at 0.5 m and 1 m sampling locations. This trend indicates that larger biological particles did not travel as far in comparison to the smaller volatiles.

Looking at all these chemical characterization methods, these results suggested that smaller volatile compounds traveled farther than larger non-volatile particles and bacteria, which settled closer to the source. These results align with the findings from the Stokes mapping experiment.

6.4 Anemometer studies

To add more context to the SPME results detailed in Chapter 6.2, the data collected in the anemometer studies were analyzed. Raw data for each of the standoff distances over 5 walking passes was plotted to determine the general trend. Examples of this raw data are shown in Figure 6.6, which shows five walking passes for each standoff distance. A moving mean filter was applied to reduce

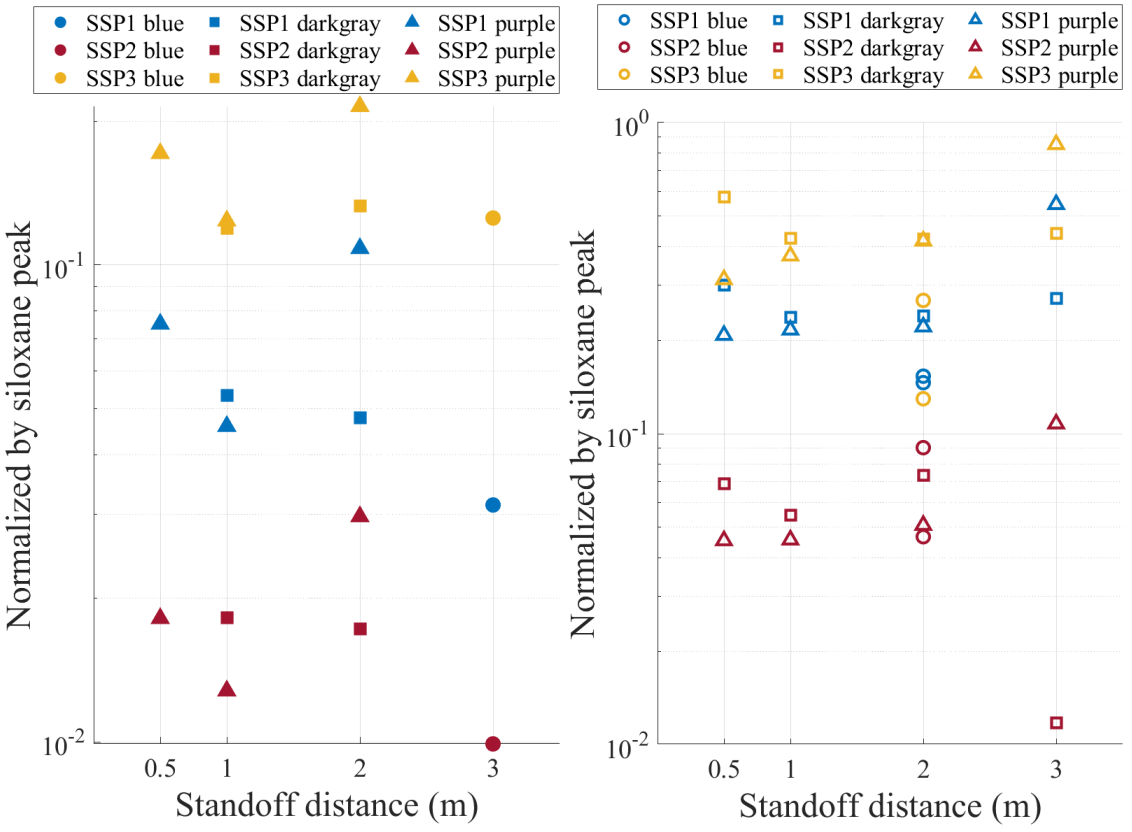

Figure 6.3: a) Relative abundance of three different sunscreen peaks over siloxane versus standoff distance in meters for 75 passes. b) Relative abundance of three different sunscreen peaks over siloxane versus standoff distance in meters for 125 passes.

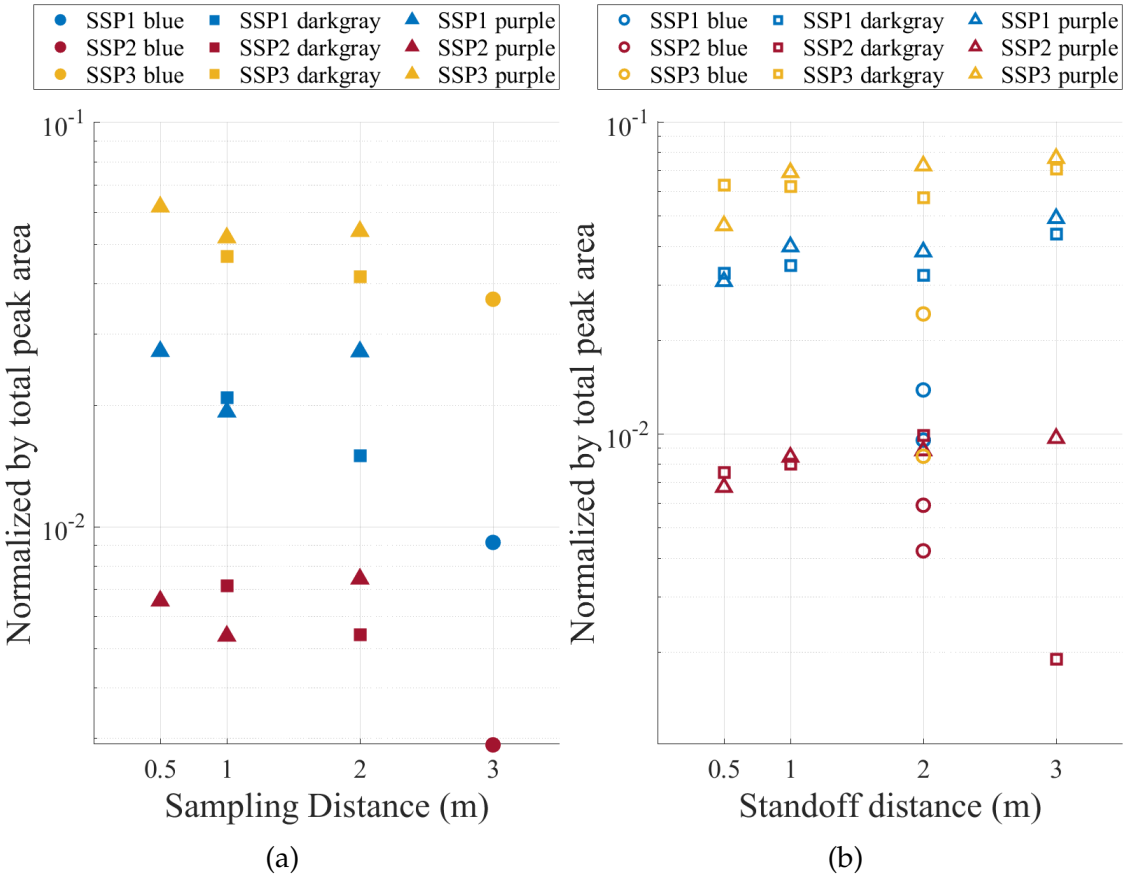

Figure 6.4: a) Relative abundance of three different sunscreen peaks over total peak area versus standoff distance in meters for 75 passes. b) Relative abundance of three different sunscreen peaks over total peak area versus standoff distance in meters for 125 passes.

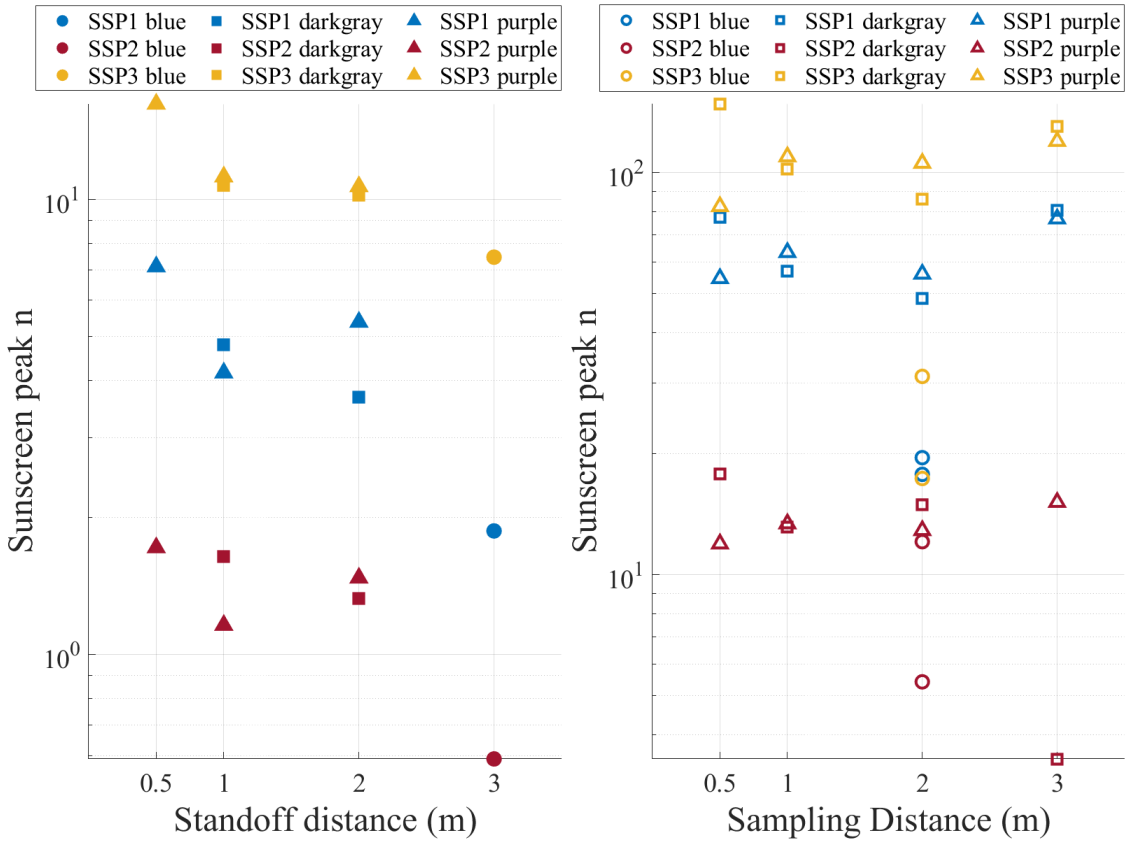

Figure 6.5: a) Peak areas of three different sunscreen peaks versus standoff distance in meters for 75 passes. b) Peak areas of three different sunscreen peaks versus standoff distance in meters for 125 passes.

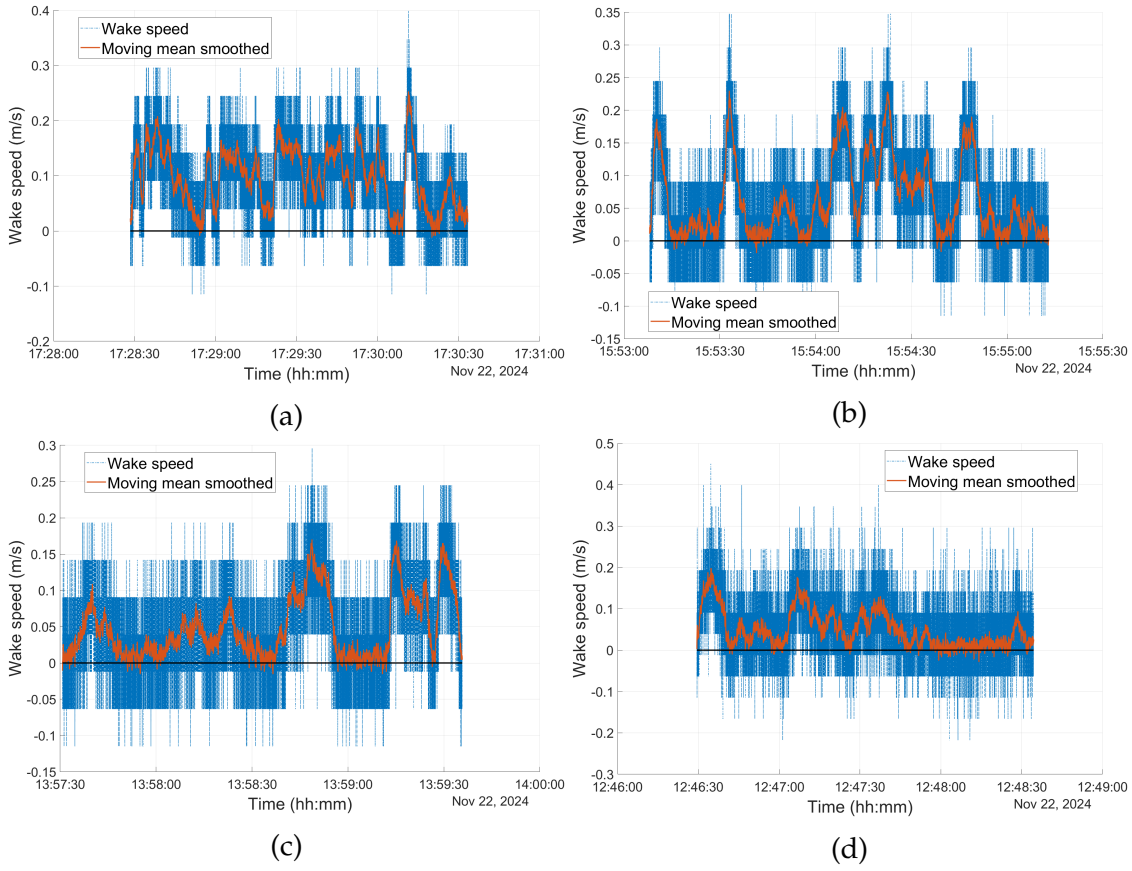

Figure 6.6: a) Example wake velocity versus time plot from anemometer readings taken over 5 walking passes at a 0.5 m standoff distance. b) Example wake velocity versus time plot from anemometer readings taken over 5 walking passes at a 1.0 m standoff distance. c) Example wake velocity versus time plot from anemometer readings taken over 5 walking passes at a 2.0 m standoff distance. d) Example wake velocity versus time plot from anemometer readings taken over 5 walking passes at a 3.0 m standoff distance.

measurement noise and better highlight trends in the signal, which is plotted in red. This was also done since this was recorded at 200 Hz, and the signal output was at 10 Hz. For each data point of interest (the central point), the filter calculates the average of 15 preceding and 15 trailing data points. The average then becomes the central point value. The process then shifts by one data point and repeats, progressively smoothing the signal over the whole data set.

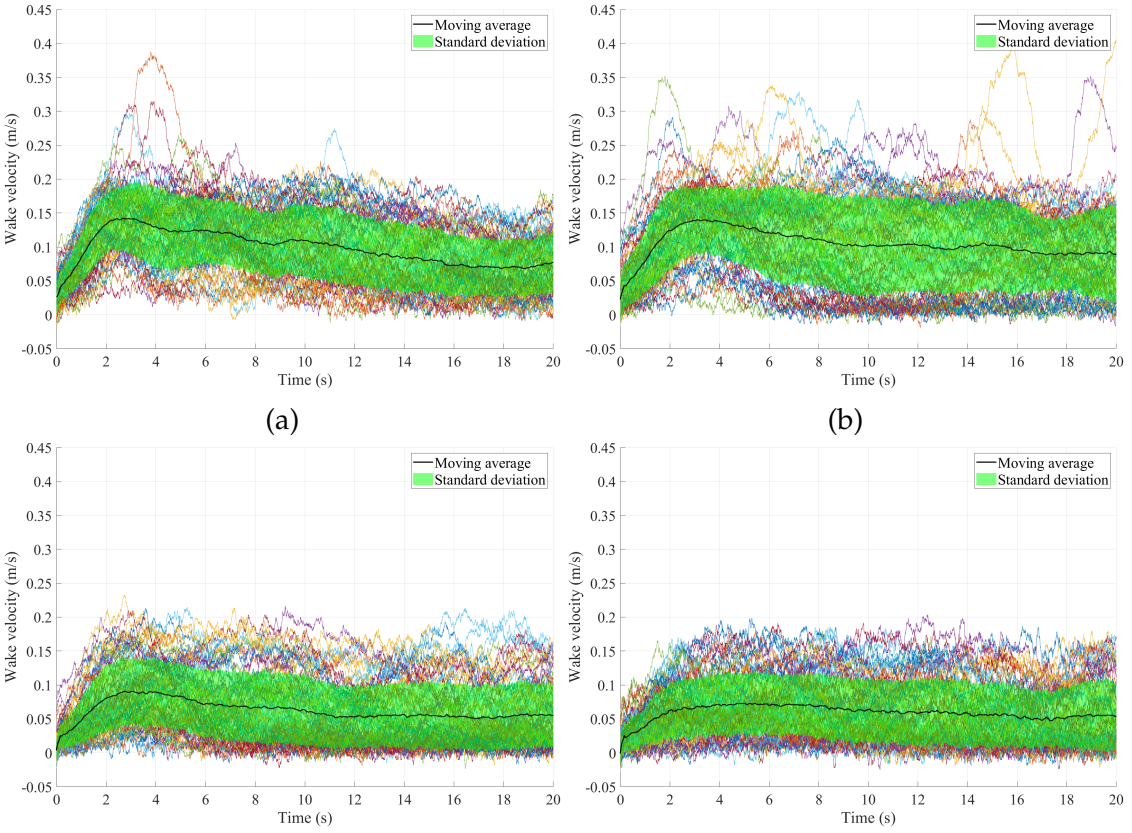

Figure 6.7: a) Wake velocity versus time for the 0.5 m standoff distance after 75 walking passes. b) Wake velocity versus time for the 1.0 m standoff distance after 76 walking passes. c) Wake velocity versus time for the 2.0 m standoff distance after 82 walking passes. d) Wake velocity versus time for the 3.0 m standoff distance after 76 walking passes.

The timestamps collected with the laser diode system were used to determine the start of each walking pass. Twenty seconds after the start was then plotted for each walking pass. The time interval between walking participants was twenty-five seconds. However, only twenty seconds were plotted to reduce the amount of data from the stall time between passes, plotted to reduce noise. With the start and time interval determined, the collected wakes were "stacked" or plotted on the same twenty-second time interval to determine trends in the

collected wake. The average velocity and standard deviation, plotted in green, of these stacked wakes were determined and also plotted. The stacked wakes for each of the standoff distances were shown in Figure 6.7.

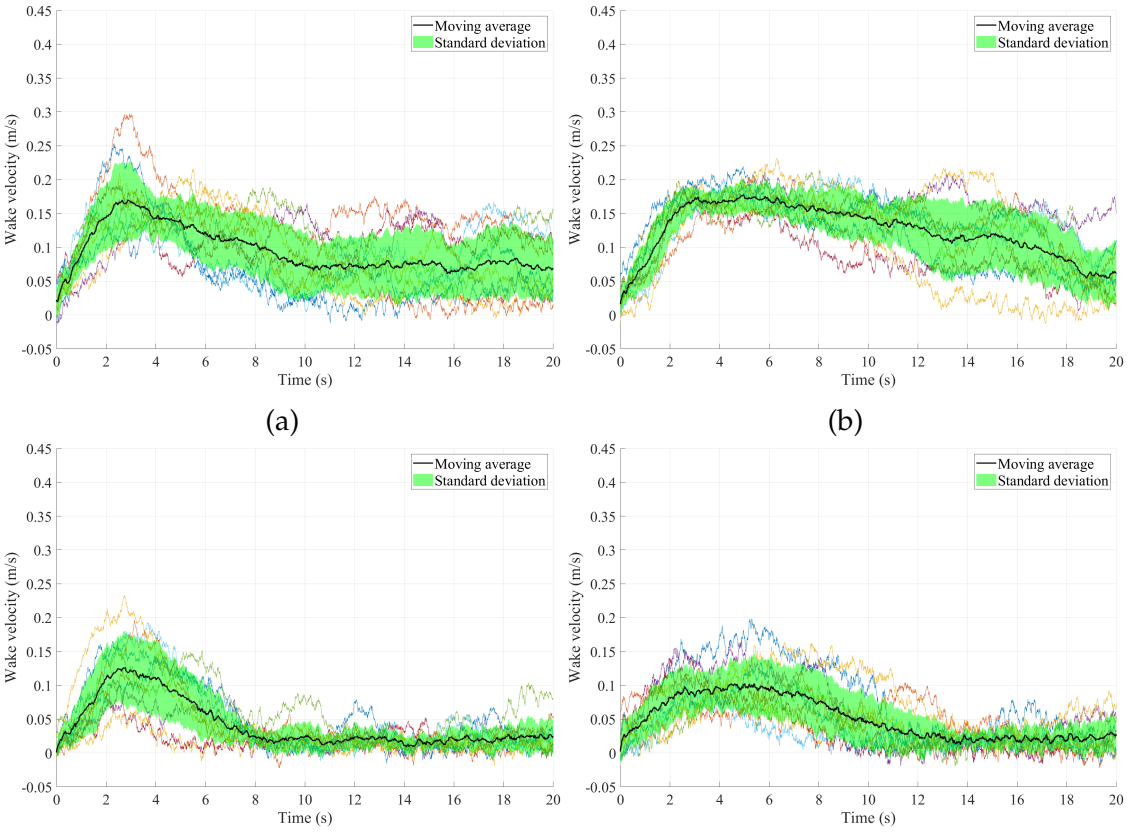

Figure 6.8: a) Wake velocity versus time for the 0.5 m standoff distance after 10 walking passes. b) Wake velocity versus time for the 1.0 m standoff distance after 10 walking passes. c) Wake velocity versus time for the 2.0 m standoff distance after 10 walking passes. d) Wake velocity versus time for the 3.0 m standoff distance after 10 walking passes.

Inspecting the average wake velocity lines in each of the graphs shown in Figure 6.7, it appears as though the velocity does not return to zero. To investigate this, ten of the best wakes from each data set were gathered and stacked as previously described to determine what was occurring here. As shown in Figure 6.8, the average wake velocity line of the 0.5 m standoff distance nearly returns to zero, and the average wake velocity lines of the 2.0 m and 3.0 m standoff distances return to zero. This trend is expected and may suggest that the reason the full data sets do not return to zero is due to noise within the data sets. However, the average velocity line for the 1.0 m standoff distance does not. Looking at Figure 6.8b, the velocity measurements vary significantly, even with the best-looking

wakes, in the later time scales. This trend may suggest the presence of other unintentional air movement through the test section or another form of measurement interference at the 1.0 m standoff location, which introduced noise to the data set that was not identified during the experiment.

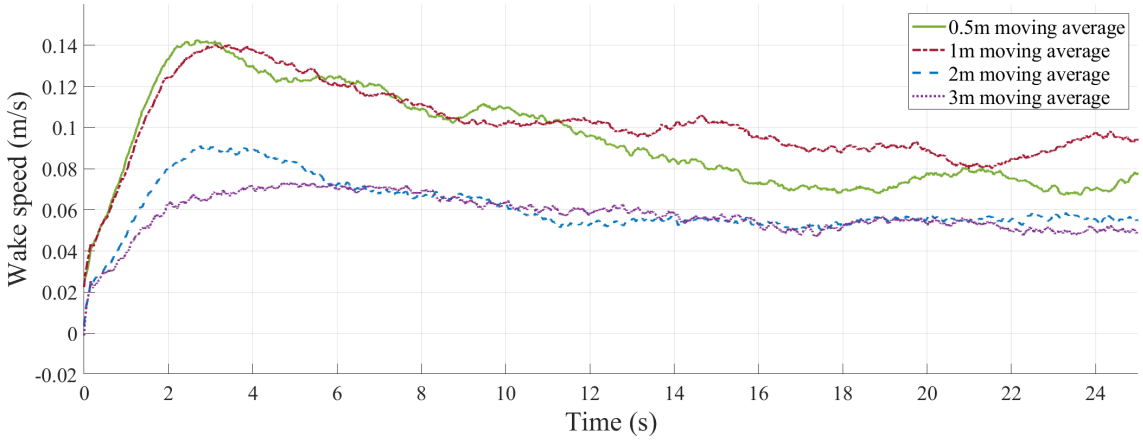

(a)

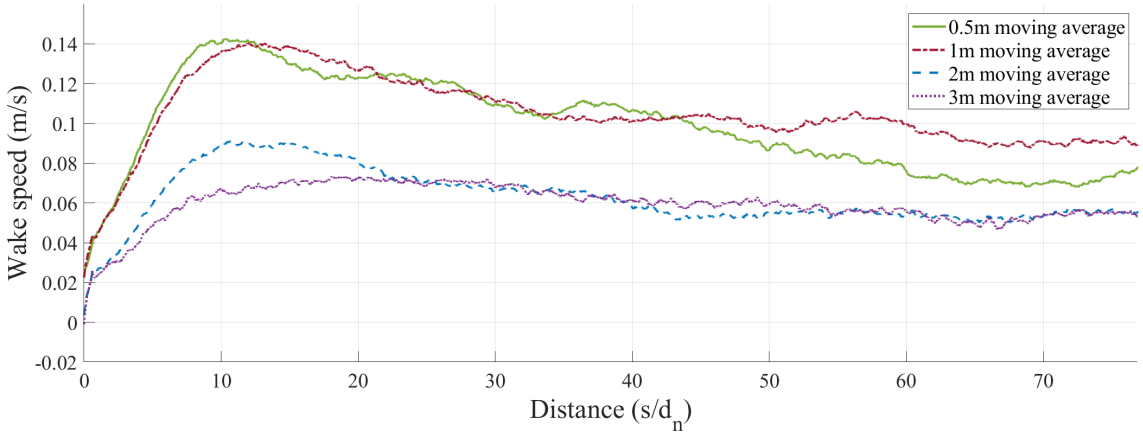

(b)

Figure 6.9: a) Wake velocity versus time in seconds at the four different standoff distances. b) Wake velocity versus normalized translated length. Length was found by multiplying the time by the walking velocity and then was normalized by the average shoulder width of the participants, where l is the test section length.

The average walking velocities found in each of the standoff cases were then plotted on the same graph for comparison, which is shown in Figure 6.9a. This plot highlights the wake decay as the standoff distance is increased.

The average walking velocity was also used to convert data from the temporal domain to the spatial domain. Previous work by Tobin and Hargather [40] demonstrated how known velocities can be used to translate results between

these domains. For this conversion, an average walking velocity of 1.58 m/s was divided by the time of a walking pass. The resulting distances were then nondimensionalized using the average shoulder width of the walking participants, which was 0.41 m, acting as the characteristic length, d_n. The final translated graph is presented in Figure 6.9b.

CHAPTER 7

SCALING BETWEEN SYSTEMS

To investigate if the two different experimental systems, the jet spray system and the walking system, are scales of each other, an investigation into the comparison between the data for both systems was conducted. For this comparison, the normalized anemometer data from the walking experiment, plotted in the spatial domain, were compared to the normalized downstream data for the final image from the jet experiment.

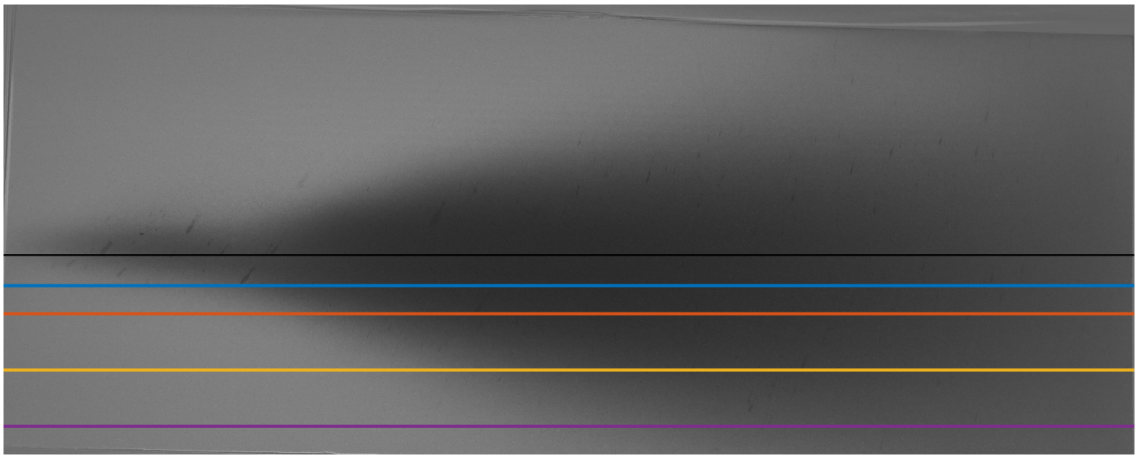

Figure 7.1: Lines drawn at nominally similar positions to the anemometer collection stations onto the jet spray image for comparison between the two systems.

In order to compare the two data sets, analysis lines were drawn on the data image in nominally similar positions to the placement of the anemometer collection stations during the walking experiment from a bird's eye view perspective of the test setup, which is shown in Figure 7.1. For this placement, the centerline of the spray was set to be the zero position as done in the axial image analysis shown in Section 5.1. Next, the nominal positions were determined by splitting two halves of the image into eight zones. The nominal 0.5 m position was placed at the border between the first and second zones. The 1 m, 2 m, and 3 m positions were placed at the border between second and third , forth and fifth, and sixth and seventh zones respectively to mimic the same spacing between the anemometer stations.

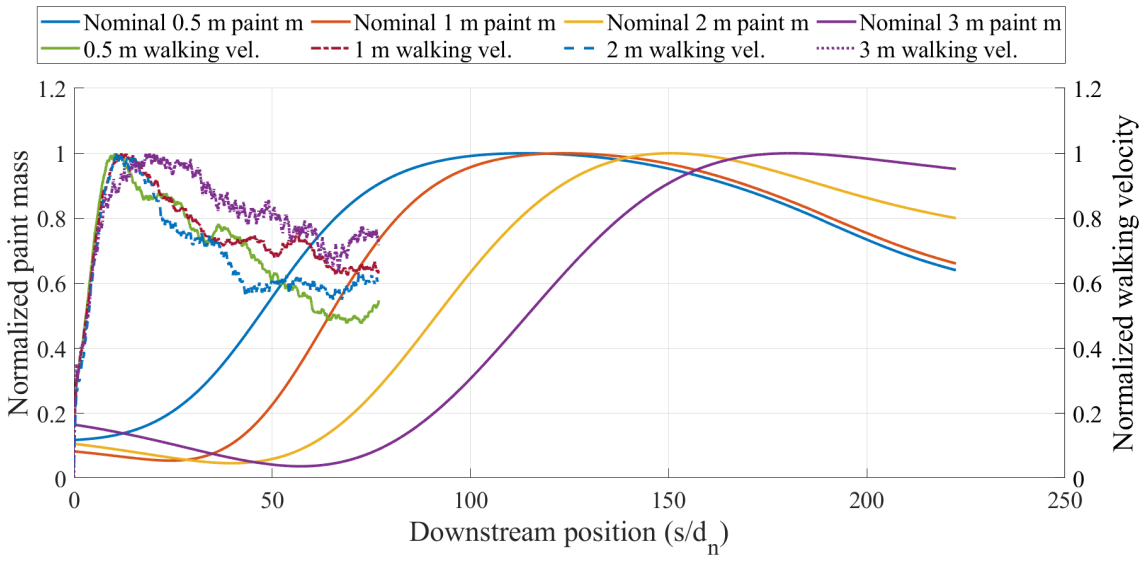

(a)

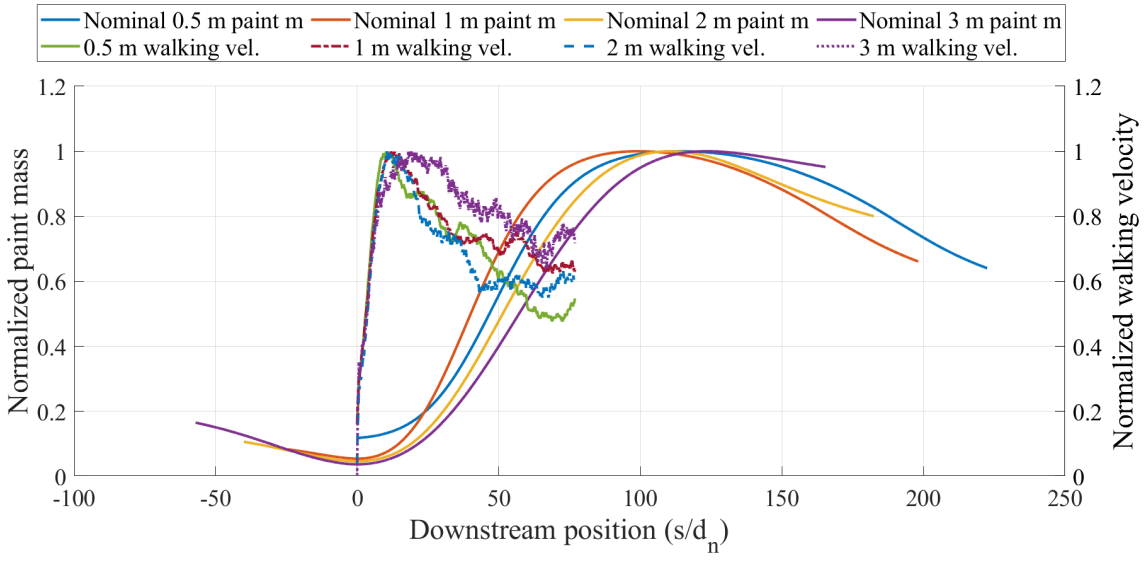

(b)

Figure 7.2: a) Plot of normalized paint mass and walking velocity versus downstream position, each scaled by its respective characteristic length. The spray jet deposition characteristic length was defined as the airbrush diameter. b) Peak-aligned plot of normalized paint mass and walking velocity versus downstream position, each scaled by its respective characteristic length. The spray jet deposition characteristic length was defined as the airbrush diameter.

With these positions established, the first comparison was done by simply plotting the results for both systems, which is shown in Figure 7.2a. As shown in the figure, the results of the comparison showed that the two data sets do not align. The peak and the decay of the anemometer data occur before the downstream data from the jet experiment reaches its peak. Leveraging Reynolds analogy, the minimum momentum transfer from the wake velocity should occur at the same point as the minimum mass transfer from the paint spray jet. The misalignment between the two data sets is most likely due to the large region before the paint deposition, where there are no intensity changes, whereas the anemometer data was plotted starting at the onset of the velocity change, which marks the beginning of the wake. To correct the minimum offset, the minima of both data sets were aligned at zero. In addition to the minima misalignment, the leading and trailing slopes between the two data sets are also misaligned. In this plot, the two slopes of the anemometer data are steeper compared to the downstream spray jet data.

Referring to the jet scaling results presented in Section 5.1, the nondimensional jet scaling relationship defined by Equation 5.1 was applied to the jet spray data to compare with the anemometer data from the walking experiment. As shown in Figure 7.3, instead of using this methodology to scale the jet spray data about the centerline of the jet, this method used the equation to scale the jet along the centerline of the jet. This scaling procedure normalizes the velocity field, making it easier to compare to the anemometer data from the walking experiment. The results is a collapse of the paint spray data closer to the origin, improving the alignment between the two data sets when compared to the unscaled data. This scaling methodology collapses data that is further from the centerline more than the data near the centerline, potentially indicating that another scaling factor is needed to account for the axial offset. However, this closer agreement reinforces the applicability of the η-based scaling approach for downstream data sets to compare to the anemometer data.

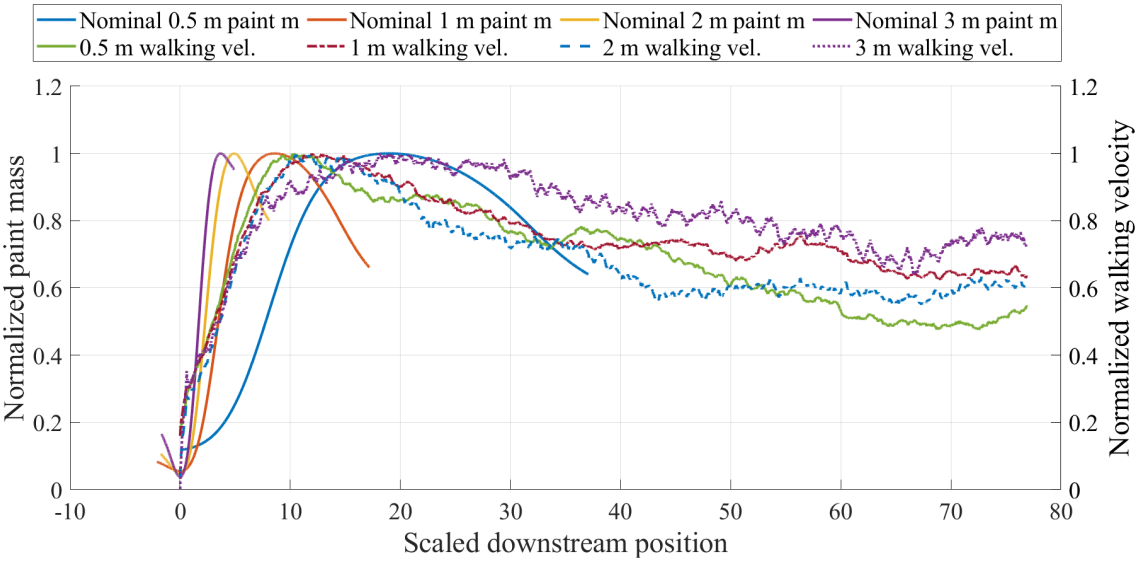

Figure 7.3: Plot of normalized paint mass and walking velocity versus scaled downstream position, each scaled with different methods in the downstream direction. The average shoulder width of the walking participants normalized walking velocity downstream position. Paint spray data was normalized by $1/\eta$.

CHAPTER 8

CONCLUSIONS AND RECOMMENDATIONS

8.1 Conclusions

The purpose of this work was to develop an understanding of how contamination spreads for the application of the results to extraterrestrial exploration, where contamination control is critical. This is because anything in the presence of humans becomes contaminated with some amount of Earthly burden [4, 8].

Buckingham Pi Theorem was applied to a jet and wake to determine the nondimensional groups that define the scenarios. The nondimensional numbers identified were the Stokes number, the Reynolds number, and the Froude number, as well as a ratio between the density of the particle and the system fluid, a ratio between the diameter of the particle and a characteristic length, and a ratio between the height of the system and a characteristic length. This nondimensionalization gave insight into the relationships between different variables in the experimental systems.

Application of known jet scaling showed that the lowest experimental height, z_0, had two separate deposition regions. Initial trends indicate that the second region to be the region of interest but more analysis is needed for validation. Additionally, height scaling was done for all three experimental heights. Paint mass was found to be proportional to pixel intensity. Microscope images taken of the paint deposition field were used to create a Stokes map. A relationship was proposed between the Stokes number and pixel intensity and used to interpolate a Stokes map for a region within the spray deposition.

Volatiles from the sunscreen were found in the SPME arrow analysis for both experimental days and at all experimental distances. Relative abundance calculations were done using siloxane, a known compound found in personal care products as well as a common contaminant, and the total area of the known peaks. The calculations showed a downward trend as the standoff distance was increased, which is in line with what Stokes number predicts. Non-volatile residues were found at the sampling stations at 0.5 m, 1 m, and 2 m after 1000 walking passes with relatively equal abundance at all distances, with a smaller amount detectable at 3 m. Microbes were found on silicon filters at 0.5 m and 1.0 m after 1000 walking passes. These different results from the three different chemical analysis techniques show that larger contaminants settle in higher concentrations closer to the walking path, whereas smaller contaminants settle throughout.

Anemometer readings from each collection scheme were averaged over all participants to form average walking velocity graphs over each experimental time interval. The average walking velocity was used to translate from the temporal domain to the spatial domain.

Scalability between a person walking through a fluid system and a paint deposition was explored using normalized average walking velocity versus distance and the downstream jet deposition versus downstream position. A relationship was found to scale between the two systems by utilizing $1/\eta$ jet scaling.

8.2 Future recommendations

Recommendations for research include developing a quantitative relationship between pixel intensity and mass of the paint deposited by the airbrush in the spray system. Developing this relationship will facilitate determining the effects on the Stokes map as the source height changes. With a more precise characterization of the changes, the methodology developed for scaling between the paint jet spray and walking systems can be applied to determine the contamination settling in the walking system. Lastly, the effects on the settling pattern when the notional geometry changes need to be explored so that the deposition maps can be applied to other contamination sources. This information would allow for the development of a scalable model to describe where contamination would settle in any environment.

Additionally, further walking experiments are required to validate the trends identified in this study. This investigation utilized siloxane and the total area of the identified peaks to ascertain relative abundance. However, it is noteworthy that siloxane was not among the identified peaks within the room standards, indicating that this volatile compound originated from the walking participants. The identification of an alternative volatile present in the room standard would substantiate the observation of a downward trend in abundance as the stand-off distance is increased. Moreover, the trends identified using the same SPME throughout the test setup would benefit from further characterization.

REFERENCES

[1] National Academies of Sciences, Engineering, and Medicine. *Origins, Worlds, and Life: A Decadal Strategy for Planetary Science and Astrobiology 2023-2032*. The National Academies Press, Washington, DC, 2022.

[2] J. T. Staley and J. J. Gosink. Poles apart: biodiversity and biogeography of sea ice bacteria. *Annual review of microbiology*, 53:189–215, 1999.

[3] Bland J. Finlay. Global Dispersal of Free-Living Microbial Eukaryote Species. *Science*, 296:1061–1063, 2002.

[4] Ron Sender, Shai Fuchs, and Ron Milo. Revised Estimates for the Number of Human and Bacteria Cells in the Body. *PLoS biology*, 14:e1002533, 2016.

[5] Brent A. Craven and Gary S. Settles. A Computational and Experimental Investigation of the Human Thermal Plume. *Journal of Fluids Engineering*, 128:1251–1258, 2006.

[6] Brian A. Edge, Eric G. Paterson, and Gary S. Settles. Computational Study of the Wake and Contaminant Transport of a Walking Human. *Journal of Fluids Engineering*, 127:967–977, 2005.

[7] Jason M. Wood, Nitin K. Singh, Lisa Guan, Arman Seuylemezian, James Nick Benardini, and Kasthuri Venkateswaran. Performance of Multiple Metagenomics Pipelines in Understanding Microbial Diversity of a Low-Biomass Spacecraft Assembly Facility. *Frontiers in microbiology*, 12:685254, 2021.

[8] Ying Zhang, Cong-Xin Xin, Lan-Tao Zhang, Yu-Lin Deng, Xiang Wang, Xiang-Yu Chen, and Zhao-Qian Wang. Detection of Fungi from Low-Biomass Spacecraft Assembly Clean Room Aerosols. *Astrobiology*, 18:1585–1593, 2018.

[9] Ryan Hendrickson, Camilla Urbaniak, Jeremiah J. Minich, Heidi S. Aronson, Cameron Martino, Ramunas Stepanauskas, Rob Knight, and Kasthuri Venkateswaran. Clean room microbiome complexity impacts planetary protection bioburden. *Microbiome*, 9:238, 2021.

[10] M. S. Race, J. E. Johnson, J. A. Spry, B. Siegel, and C. A. Conley. Planetary Protection Knowledge Gaps for Human Extraterrestrial Missions: Workshop Report. techreport DAA_TN36403, NASA Ames Research Center, Moffett Field, CA, 2015.

[11] Edgar Buckingham. On Physically Similar Systems; Illustrations of the Use of Dimensional Equations. *Phys. Rev.*, 4:345–376, 1914.

[12] Osborne Reynolds. An Experimental Investigation of the Circumstances Which Determine Whether the Motion of Water Shall Be Direct or Sinuous, and of the Law of Resistance in Parallel Channels. *Philosophical Transactions of the Royal Society of London*, 174:935–982, 1883.

[13] William Froude. On the Rolling of Ships. *Transactions of the Institution of Naval Architects*, 2:180–227, 1861.

[14] Arsath Abbasali Ayubali, Balasivanandha Prabu Shanmugavel, and K.A. Padmanabhan. On material-agnostic fatigue life prediction using Buckingham Pi Theorem. *Engineering Fracture Mechanics*, 280:109021, 2023.

[15] Allen L. Garner and Keith Lewis. Buckingham pi analysis of railgun multiphysics. *IEEE Transactions on Plasma Science*, 42(8):2104–2112, 2014.

[16] Na Luo, Wenguo Weng, Xiaoyu Xu, and Ming Fu. Experimental and numerical investigation of the wake flow of a human-shaped manikin: experiments by PIV and simulations by CFD. *Indoor and Built Environment*, 2017.

[17] Yao Tao, Kiao Inthavong, and Jiyuan Tu. A numerical investigation of wind environment around a walking human body. *Journal of Wind Engineering and Industrial Aerodynamics*, 168:9–19, 2017.

[18] Brian A. Edge. Computational Fluid Dynamics Simulation of the Human Aerodynamic Wake. Master's thesis, The Pennsylvania State University, 2003.

[19] Brent A. Craven, Michael J. Hargather, Jason A. Volpe, Stephen P. Frymire, and Gary S. Settles. Design of a High-Throughput Chemical Trace Detection Portal That Samples the Aerodynamic Wake of a Walking Person. *IEEE Sensors Journal*, 14(6):1852–1866, 2014.

[20] Jason A. Volpe. The Design of an Aerodynamic Wake Sampling Portal . Master's thesis, The Pennsylvania State University, December 2007.

[21] Wygnanski I and Fiedler HE. The two-dimensional mixing region. *Journal of Fluid Dynamics*, 41(2):327–361, 1970.

[22] Paweł A. Kluza, Izabela Kuna-Broniowska, and Stanisław Parafiniuk. Modeling and Prediction of the Uniformity of Spray Liquid Coverage from Flat Fan Spray Nozzles. *Sustainability*, 11(23):6716, 2019.

[23] Yao Tao, Kiao Inthavong, and Jiyuan Tu. CFD study of human-induced wake and particle dispersion in indoor environment. *Indoor and Built Environment*, 26(2):185–198, 2016.

[24] Wayne Smith. Dispersion of a Chemical Plume From a Container in Crossflow. Master's thesis, The Pennsylvania State University, December 2005.

[25] Michael J. Hargather, Matthew E. Staymates, Matthew J. Madalis, Daniel J. Smith, and Gary S. Settles. The Internation Aerodynamics of Cargo Containers for Trace Chemical Sampling and Detection. *IEEE Sensors Journal*, 11(5):1184–1193, 2011.

[26] P. J. Samson. Atmospheric transport and dispersion of air pollutants associated with vehicular emissions. In A. Y. Watson, R. R. Bates, and D. Kennedy, editors, *Air Pollution, the Automobile, and Public Health*. National Academies Press (US), Washington, DC, 1988.

[27] Janusz Pawliszyn. *Solid Phase Microextraction: Theory and Practice*. Wiley-VCH, 1997.

[28] Muhammad Sajid, Mazen Khaled Nazal, Malgorzata Rutkowska, Natalia Szczepanka, Jacek Namiesnik, and Justyna Plotka-Wasylka. Solid Phase Microextraction: Apparatus, Sorbent, Materials, and Application. *Critical Reviews in Analytical Chemistry*, 49(3):271–288, 2018.

[29] Vahid Jalili, Abdullah Barkhordari, and Alireza Ghiasvand. A comprehensive look at solid-phase microextraction technique: A review of reviews. *Microchemical Journal*, 152:104319, 2020.

[30] Jason S. Herrington, German A. Gómez-Ríos, Colton Myers, Gary Stidsen, and David S. Bell. Hunting Molecules in Complex Matrices with SPME Arrows: A Review. *Separations*, 7(1):12, 2020.

[31] Helena Prosen and Lucija Zupančič-Kralj. Solid-phase microextraction. *Trends in Analytical Chemistry*, 18(4):272–282, 1999.

[32] Zhouyao. Zhang and Janusz. Pawliszyn. Headspace solid-phase microextraction. *Analytical Chemistry*, 65(14):1843–1852, 1993.

[33] R. S. Gohlke. Time-of-flight mass spectrometry and gas-liquid partition chromatography. *Anal. Chem.*, 31(4):535–541, 1959.

[34] Fulton G. Kitson. *Gas Chromatography and Mass Spectrometry*. Elsevier Science & Technology, San Diego, 1st ed. edition, 1996.

[35] Eugene N. Borson, Ethel J. Watts, and Gloria A. To. Standard Method for Measurement of Nonvolatile Residue on Surfaces. 1989.

[36] A. Petrosyan, B. Galperin, S. E. Larsen, S. R. Lewis, A. Määttänen, P. L. Read, N. Renno, L. P. H. T. Rogberg, H. Savijärvi, T. Siili, A. Spiga, A. Toigo, and L. Vázquez. The martian atmospheric boundary layer. *Rev. Geophys.*, 49(3), September 2011.

[37] Pijush K. Kundu and Ira M. Cohen. *Fluid mechanics*. Elsevier Academic Press, Amsterdam, 3. ed., [repr.] edition, 2006.

[38] E.-U. Schlünder. Analogy between heat and momentum transfer1dedicated to professor k.r. westerterp on the occasion of his 70th birthday.1. *Chemical Engineering and Processing: Process Intensification*, 37(1):103–107, 1998.

[39] Hussein J. Hussein, Steven P. Capp, and William K. George. Velocity measurements in a high-Reynolds-number, momentum-conserving, axisymmetric, turbulent jet. *Journal of Fluid Mechanics*, 258:31–75, 1994.

[40] Jesse D. Tobin and Michael J. Hargather. Quantitative Schlieren Measurement of Explosively-Driven Shock Wave Density, Temperature, and Pressure Profiles. *Propellants, Explosives, Pyrotechnics*, 41(6):1050–1059, 2016.

A STATISTICAL STUDY OF THE CONTAMINANT DEPOSITION FROM A JET AND BEHIND A MOVING PERSON

by

Autumn Noël Weber